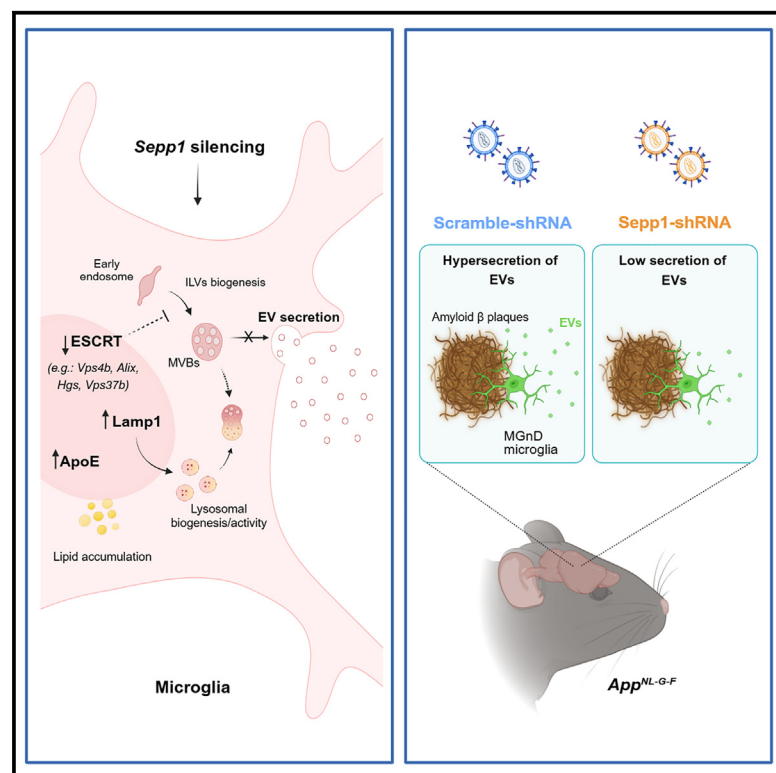


# Selenoprotein P is a target for regulating extracellular vesicle biogenesis and secretion from activated microglia *in vivo*

## Graphical abstract



## Authors

Victor Bodart-Santos, Zhi Ruan, Bridgette C. Melvin, Ikshu Pandey, Seiko Ikezu, Tsuneya Ikezu

## Correspondence

ikezu.tsuneya@mayo.edu

## In brief

Bodart-Santos et al. show that *Sepp1* is a key regulator of ATP-induced secretion of EVs by microglia. *Sepp1*-deficient microglia show impairment in expression of genes associated with EV biogenesis machinery and display increased lysosomal activity. Downregulation of *Sepp1* halts hypersecretion of EVs by amyloid plaque-associated MGnD microglia.

## Highlights

- Selenoprotein P (*Sepp1*) is a regulator of microglia EV secretion
- Downregulation of *Sepp1* impacts endolysosomal pathways and EV biogenesis
- *Sepp1* deficiency leads to increased lipid accumulation and lysosomal activity in microglia
- *Sepp1* silencing reduces EV secretion from neurodegenerative (MGnD) microglia in *APP<sup>NL-G-F</sup>* mice



## Article

# Selenoprotein P is a target for regulating extracellular vesicle biogenesis and secretion from activated microglia *in vivo*

Victor Bodart-Santos,<sup>1</sup> Zhi Ruan,<sup>1</sup> Bridgette C. Melvin,<sup>1</sup> Ikshu Pandey,<sup>2</sup> Seiko Ikezu,<sup>1</sup> and Tsuneya Ikezu<sup>1,3,4,5,6,\*</sup><sup>1</sup>Department of Neuroscience, Mayo Clinic Florida, Jacksonville, FL 32224, USA<sup>2</sup>Whiting School of Engineering, Johns Hopkins University, Baltimore, MD 21218, USA<sup>3</sup>Regenerative Science Graduate Program, Mayo Clinic College of Medicine, Jacksonville, FL 32224, USA<sup>4</sup>Robert and Alene Kogod Center on Aging, Mayo Clinic, Jacksonville, FL 32224, USA<sup>5</sup>Alzheimer's Disease Research Center, Mayo Clinic, Jacksonville, FL 32224, USA<sup>6</sup>Lead contact\*Correspondence: [ikezu.tsuneya@mayo.edu](mailto:ikezu.tsuneya@mayo.edu)<https://doi.org/10.1016/j.celrep.2024.115025>

## SUMMARY

Microglia, brain innate immune cells, participate in the spread of inflammatory signals and aggregated proteins through secretion of extracellular vesicles (EVs). Selenoprotein P (Sepp1) is a potential regulator of microglial EV secretion. Here, we investigate the effect of *Sepp1* silencing on microglial transcriptomics to elucidate the *Sepp1* regulatory mechanism of EV secretion and validate this effect in *APP<sup>NL-G-F</sup>* knockin mice. Silencing of *Sepp1* significantly reduces EV secretion and CD63 loading to EVs from BV-2 microglia, as determined by single-vesicle flow cytometry and super-resolution microscopy. *Sepp1* deficiency down-regulates EV biogenesis machinery, accompanied by increased lysosomal activity and lipid metabolism. Silencing of *Sepp1* in astrocytes but not neurons suppresses EV secretion *in vitro*. Finally, *Sepp1* silencing reduces EV secretion from activated neurodegenerative microglia associated with amyloid plaques in *APP<sup>NL-G-F</sup>* mouse brains *in vivo*. *Sepp1* is thus an emerging therapeutic target for ameliorating microglia-mediated disease spread through EV secretion in neurodegenerative disorders.

## INTRODUCTION

Microglia are innate immune cells originating from the myeloid lineage that reside in the central nervous system (CNS). Microglia have important functions in immune surveillance and maintenance of physiological activities of neurons, participating in processes related to synaptic pruning and neuronal plasticity.<sup>1,2</sup> Microglia continuously survey the CNS environment and respond to pathological stimuli. Upon activation, microglia extend their ramified processes for phagocytosis of pathogens, dead cells, and protein aggregates.<sup>3</sup> Microglial activation is followed by expression of pro- and anti-inflammatory chemokines, which can contribute to neuroinflammation and has been widely observed in neurodegenerative diseases, such as patients with Alzheimer's disease (AD).<sup>4,5</sup> Recent advances in phenotypic characterization of microglia in patients with AD have provided new insights into the molecular mechanisms involved in microglial activation. These studies revealed a neurodegenerative or disease-associated microglia phenotype (MGnD or DAM, respectively), and whether the effects of these phenotypes are beneficial or harmful in neurodegeneration remains under debate.<sup>6–8</sup>

In the brain of AD animal models, microglia surrounding amyloid plaques exhibit an MGnD phenotype.<sup>6,9</sup> In *APP<sup>NL-G-F</sup>* mice, a humanized *APP* knockin mutant mouse model that displays a

robust  $\beta$ -amyloid (A $\beta$ ) burden, MGnD microglia appear to actively contribute to tau propagation in a process involving increased biogenesis and secretion of extracellular vesicles (EVs), which can contain phosphorylated tau.<sup>9</sup> EVs are nanoscale membranous vesicles secreted by cells comprising exosomes and microvesicles and play a pivotal role in intercellular communication. EVs carry a wide range of bioactive molecules, including nucleic acids, proteins, lipids, and metabolites, which could be dynamically altered in response to environmental changes, including pathological signals.<sup>10–13</sup> Several extracellular stimuli, such as ATP, a molecule that accumulates extracellularly at damaged tissues or during inflammation, and lipopolysaccharide (LPS), have been reported to activate microglia and induce secretion of EVs.<sup>14–16</sup> These stimuli can increase the release of inflammatory molecules such as interleukin-1 $\beta$  (IL-1 $\beta$ ) on EVs, promoting the propagation of neuroinflammatory responses in the CNS.<sup>17,18</sup> Intriguingly, EVs isolated from postmortem brain parenchyma tissue of patients with AD have been shown to carry A $\beta$  and tau protein and tau seeding activity and induce cognitive impairment in mice.<sup>19,20</sup> These findings align with previous reports showing that microglia can take up and secrete tau in EVs more efficiently than neurons and astrocytes.<sup>21</sup> Thus, EVs secreted by activated microglia can potentially contribute to the spread of pathological molecules in the brain, and new ways to specifically modulate EV secretion by microglia may serve as potential therapy for



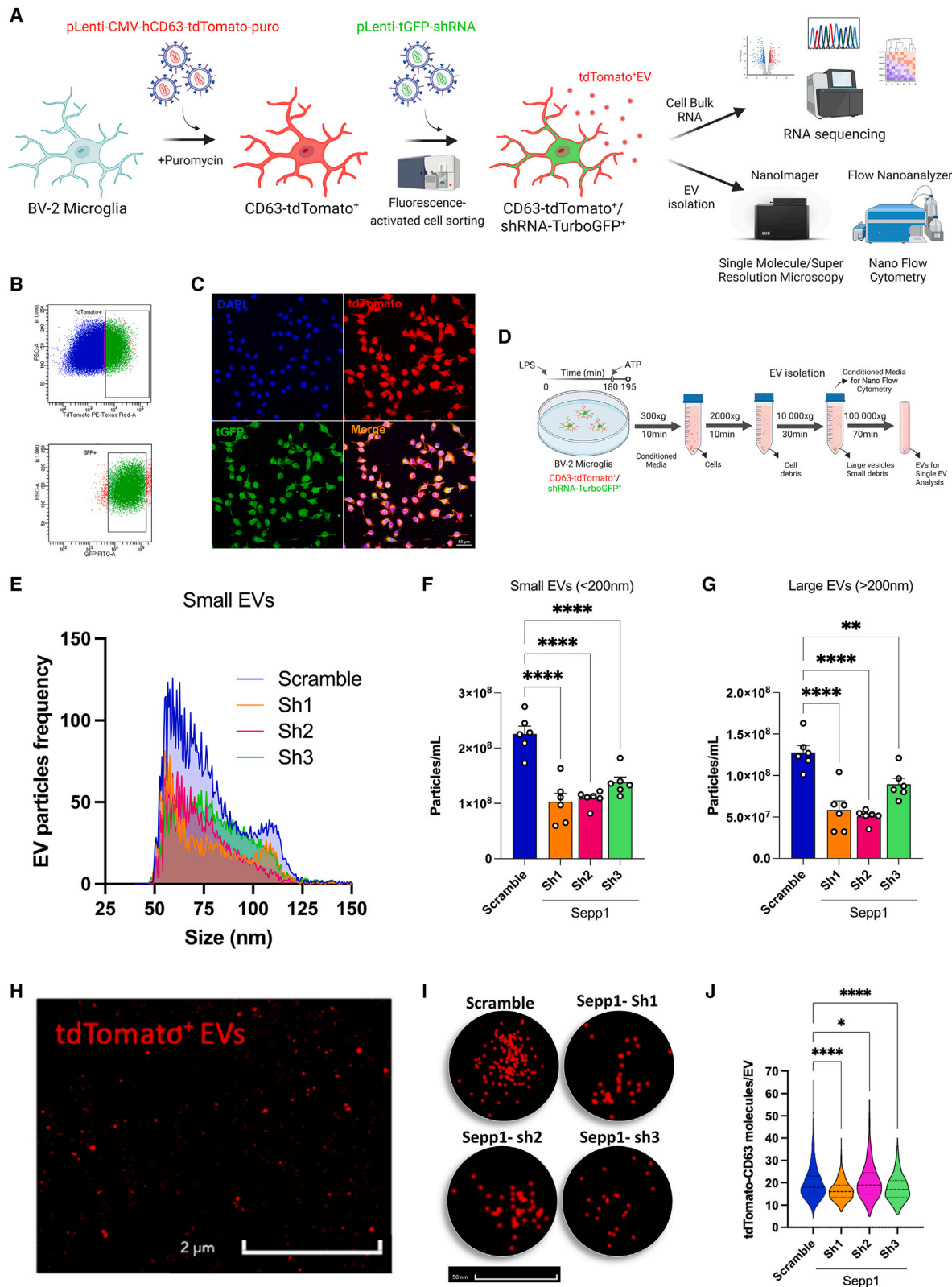


**Figure 1. Generation of the microglia BV-2 EV reporter to monitor the effects of *Sepp1* downregulation and EV secretion**

(A) Schematic of the protocol for generation of tdTomato-CD63<sup>+</sup> BV-2 cells and lentivirus-induced expression of tGFP-shRNA targeting *Sepp1*, created with BioRender.

(legend continued on next page)

targeting neuroinflammation and neurodegenerative diseases, including AD.

In this study we investigate the effect of selenoprotein P (*Sepp1*) silencing in microglia, a gene corresponding to a secreted heparin-binding glycoprotein, which we have recently identified as a potential regulator of EV secretion from both BV-2 microglial cells and primary microglia under pro-inflammatory and ATP stimulation.<sup>22</sup> *Sepp1* is highly expressed in the liver and represents a major selenoprotein found in the plasma.<sup>23–25</sup> *Sepp1* function has been mainly associated with selenium binding and transport to different tissues, including as an EV cargo to deliver selenium to neuronal cells, as well as antioxidant properties.<sup>26–28</sup> We employed a short hairpin RNA (shRNA) for targeting *Sepp1* expression and analyze microglial EV secretion *in vitro* and in *APP<sup>NL-G-F</sup>* mice *in vivo*. Using these models, we show that silencing of *Sepp1* reduces EV secretion from MGnD microglia affecting EV biogenesis and secretory machineries at transcriptional levels. The findings presented here provide insights regarding targeting *Sepp1* for dampening microglia-EV biogenesis and secretion, which may lead to suppression of disease progression.

## RESULTS

### *Sepp1* silencing affects EV secretion and loading in BV-2 microglia

To monitor the effects of *Sepp1* silencing on microglia and EVs, we used a mouse immortalized microglial BV-2 cell line. BV-2 cells exhibit phagocytic ability,<sup>29</sup> and we have shown previously that they express the TREM2 and TYROBP2, microglial markers<sup>30</sup> and secrete IL-1 $\beta$  in response to LPS+ATP stimulation.<sup>22</sup> In this study, we transduced BV-2 microglial cells with a lentiviral construct for expression of CD63-tdTomato (Figure 1A), as described previously.<sup>22</sup> After puromycin selection, CD63-tdTomato<sup>+</sup> cells were expanded and transduced with a lentiviral construct expressing TurboGFP (tGFP) and shRNA (clones 1–3) targeting *Sepp1* or scramble. Double-positive cells expressing CD63-tdTomato<sup>+</sup>/tGFP-shRNA<sup>+</sup> were sorted by fluorescence-activated cell sorting (FACS) (Figure 1B) and further expanded for functional assays. To investigate the effects of *Sepp1* silencing in microglial EV secretion, we tested the effect of three different clones of tGFP-shRNA targeting *Sepp1* in tdTomato-CD63<sup>+</sup> cells (Figure 1C). *Sepp1*-shRNA transduced cells showed 77.64%  $\pm$  8.79% reduction in *Sepp1* expression (Figure S1A). While LPS can enhance EV secretion, ATP can promote a fast release of CD63<sup>+</sup> EV particles by microglia within 15 min after

exposure.<sup>22</sup> After stimulation with LPS and ATP, EVs were isolated from conditioned medium (CM) by sequential centrifugation and ultracentrifugation (Figure 1D). We assessed the concentration of small (<200 nm) and large (>200 nm) EVs secreted in CM from CD63-tdTomato<sup>+</sup>/tGFP-shRNA<sup>+</sup> BV-2 cells using a flow nanoanalyzer (NanoFCM). The microglial EVs presented a similar size distribution range among groups, with an enrichment of particles 40–150 nm in diameter (Figures 1E and S1B–S1F). The number of small and large EVs secreted in CM by microglia was strongly reduced ( $\sim$ 50%) by all *Sepp1*-shRNA clones compared to the scramble-shRNA control group (Figures 1F and 1G). Additionally, we quantified the number of single CD63-tdTomato<sup>+</sup> molecules loaded on EVs isolated from CM by direct stochastic optical reconstruction microscopy using the Nanoimager system (ONI; Figure 1H). The number of tdTomato<sup>+</sup> molecules per single EV was significantly reduced by *Sepp1*-shRNA1 and shRNA3 and increased by shRNA2 (Figures 1I and 1J). These results suggest that *Sepp1* silencing has robust effects on EV secretion and membrane cargo loading, as represented by CD63 in microglia.

### Transcriptomics analysis of *Sepp1* silencing on BV-2 microglia

To better understand the effects of *Sepp1* downregulation in microglia, we performed bulk RNA sequencing to compare three *Sepp1*-shRNA BV-2 clones. Bioinformatic analysis of *Sepp1*-shRNA clones provides good correlation and clustering among the different shRNA BV-2 clones (Figures 2A and 2B). Volcano plots displaying the differentially expressed genes (DEGs) showed that *Sepp1* downregulation by different shRNA clones can differentially affect gene expression in BV-2 microglial cells (Figures 2C–2E; Table S1). A Venn diagram showed that there were 235 significantly upregulated and 82 significantly downregulated DEGs that were commonly regulated by all *Sepp1*-shRNA clones. One example is the apolipoprotein E (*ApoE*) gene, which was upregulated in response to *Sepp1* silencing (Figure 2F). Gene Ontology annotation using DEGs that overlap with at least two *Sepp1*-shRNA clones provided classification of the main cellular components, biological process, and molecular function of genes regulated by *Sepp1* downregulation (Figure 2G). A cluster of genes relating to organelles and membranes represented the main cellular component. Binding and catalytic activity are the major biological processes. Regulation of cellular metabolism and response to stimulus are the highest molecular functions associated with *Sepp1* downregulation.

(B) Transduced tdTomato-CD63<sup>+</sup> tGFP-shRNA<sup>+</sup> BV-2 cells were sorted by FACS.

(C) Representative images of double-positive (tdTomato<sup>+</sup>/tGFP<sup>+</sup>) BV-2 cells transduced with tGFP-shRNA for downregulation of *Sepp1*. Scale bar, 50  $\mu$ m.

(D) Workflow for purification of EVs from the conditioned medium (CM) of tdTomato-CD63<sup>+</sup> BV-2 microglia upon stimulation with LPS and ATP; created with BioRender.

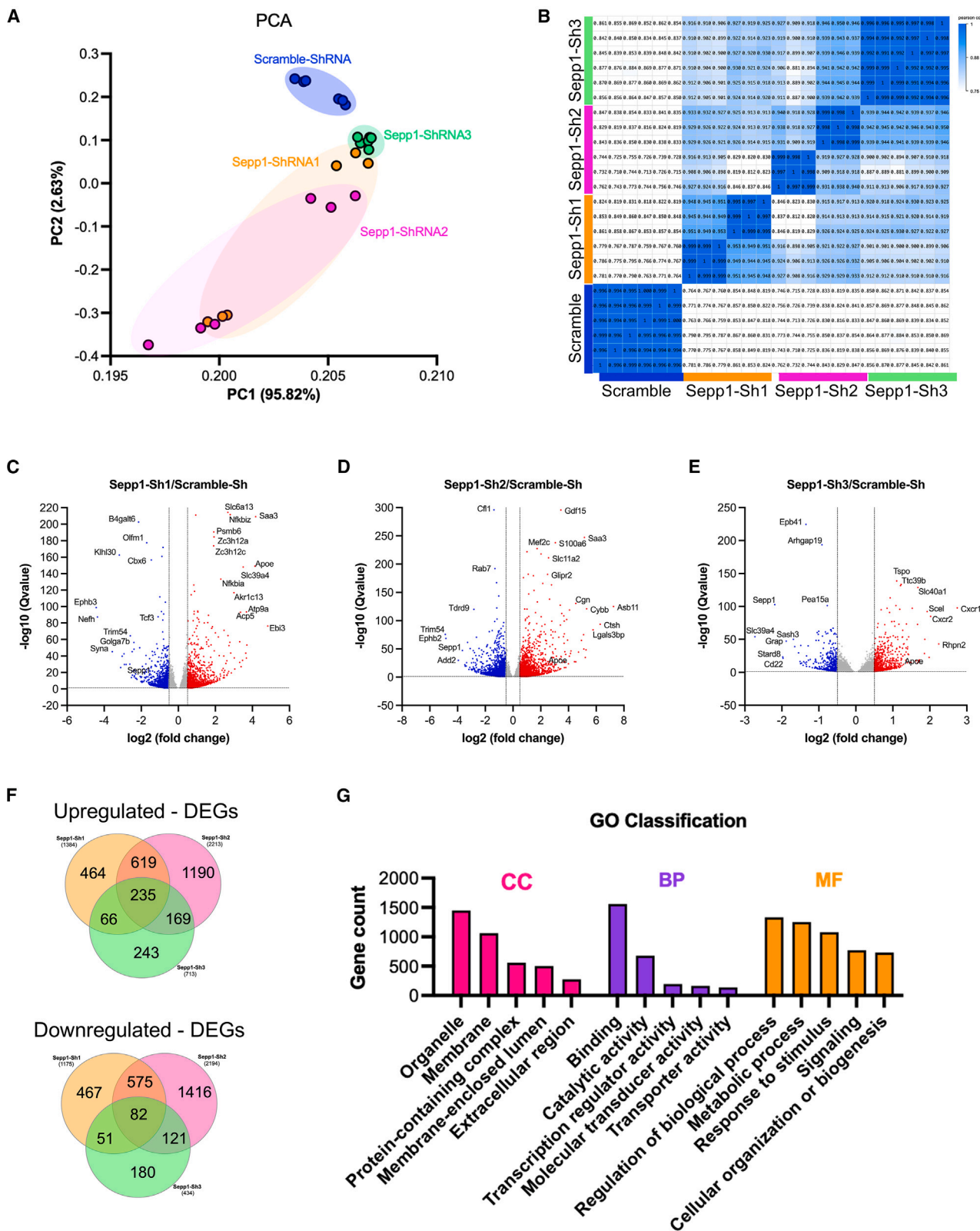
(E–G) Size distribution and concentration of EVs secreted on CM of BV-2 cells were measured by nanoflow cytometry using a flow nanoanalyzer (NanoFCM); \*\* $p$  < 0.01 and \*\*\*\* $p$  < 0.0001 by one-way ANOVA with Holm-Sidak post hoc analysis ( $n$  = 6 replicates per group). The assessment of tdTomato-CD63<sup>+</sup> molecule loading on EVs was performed using the Nanoimager system (ONI).

(H) Representative image of single tdTomato-CD63<sup>+</sup> EVs. Scale bar, 2  $\mu$ m.

(I and J) Single-molecule fluorescence analysis of tdTomato-CD63 loading on EVs was performed at single-EV level, and the number of tdTomato-CD63 molecules present in single EVs was quantified using the CODI platform from ONI; one-way ANOVA with Holm-Sidak post hoc analysis ( $n$  = 3 replicates per group).

\* $p$  < 0.05, \*\* $p$  < 0.01, and \*\*\*\* $p$  < 0.0001 by one-way ANOVA with Holm-Sidak post hoc analysis ( $n$  = 6 per group). Scale bar, 50 nm. Data are represented as mean  $\pm$  SEM.





(legend on next page)

### Downregulation of *Sepp1* impacts endolysosomal pathways and disrupts intraluminal vesicle biogenesis

Silencing of *Sepp1* induced downregulation of several EV-related genes, such as *Cd63*, by all *Sepp1*-shRNAs, *Cd9* expression by *Sepp1*-shRNA2, *Flot1* expression by *Sepp1*-shRNA2 and shRNA3, and *Flot2* expression by *Sepp1*-shRNA1 and shRNA2 (Figure S2A). Silencing of *Sepp1* also significantly suppressed phagocytosis of phRodo-labeled bioparticles (Figure S3A), demonstrating its effect on microglial phagocytosis. To investigate the role of *Sepp1* in EV biogenesis in microglia, we performed pathway analysis based on the Kyoto Encyclopedia of Genes and Genomes (KEGG) database using commonly regulated DEGs among the *Sepp1*-shRNA clones. From the top 10 cellular processes associated with this dataset, we identified a cluster of genes associated with endocytosis and lysosome pathways (Figure 3A). Interestingly, the endocytosis machinery contains several accessory or component genes of the endosomal sorting complex required for transport (ESCRT), such as *Vps4b*, *Hgs*, *Vps37b*, *Mvb12b*, and *Chmp2b*, which are part of EV biogenesis pathways and were downregulated by *Sepp1*-shRNA (Figures 3B and 3C). The expression level of ESCRT-accessory *Alix* was also significantly reduced by *Sepp1*-shRNA (Figure 3C). Another set of genes that are associated with the retromer complex of endosomal cargo sorting, such as *Rab11b*, *Snx6*, and *Vps26a*, was also downregulated (Figures 3B and 3D). On the other hand, *Sepp1* silencing enhances the lysosomal pathway with increased expression of *Lamp1*, a gene encoding to a highly enriched lysosomal membrane protein and playing an important role in lysosome activity (Figures 3B and 3E). Taken together, these data show that silencing of *Sepp1* induces downregulation of genes related to endosomal machinery and EV biogenesis along with upregulation of genes related to lysosomal function. These data suggest that *Sepp1* regulates EV secretion by modulating EV synthesis, which is negatively associated with lysosomal activity.

### *Sepp1* affects lipid metabolism and inter/intracellular trafficking pathways

Further analysis using highly up- and downregulated DEGs (fold change  $\geq +1$  or  $\leq -1$ ;  $q < 0.05$ ) by *Sepp1*-shRNA showed upregulation of the lipoproteins *Saa3* and *Apoe* as well as the mitochondrial translocator protein gene *Tspo*, a widely used marker to assess microglial activation *in vivo*. The cell membrane glutamate transporter *Slc1*, the calcium downstream effector *Camkk1*, heparan sulfate proteoglycan 2 (*Hspg2*), and the signaling receptor and transporter of retinol *Stra6* comprise the genes downregulated by *Sepp1*-shRNA (Figure 4A). Despite the increased

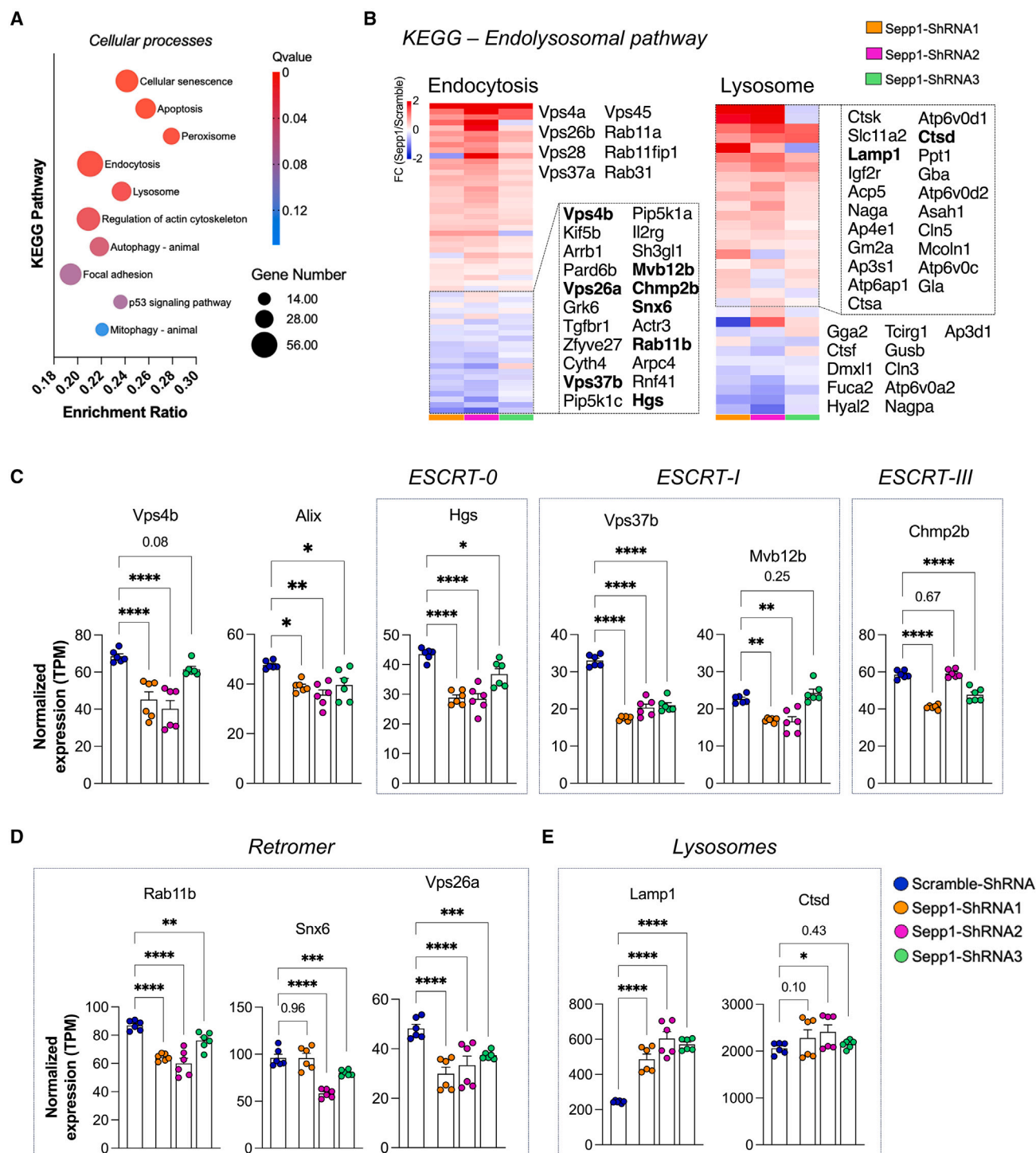
*Apoe* expression, we did not observe a clear upregulation of MGnD genes in comparison with homeostatic microglia genes by *Sepp1*-shRNA (Figure S3B). Enriched pathway analysis of these DEGs showed association with regulation of immunity, intracellular transport and cell secretion, receptor-mediated endocytosis, and fatty acid metabolism (Figure 4B; Table S2). Ingenuity Pathway Analysis (IPA) of the gene set identified downregulation of the liver X receptor/retinoid X receptor (LXR/RXR) pathway, which is strongly related to lipoprotein synthesis, cholesterol transport, lipogenesis, and inflammatory mediators (Figures 4C and S4). Complementary IPA analysis aiming for the top predicted biological effectors and their interactions identified NPC intracellular cholesterol transporter 1 (*Npc1*), prostaglandin E receptor 4 (*Ptger4*), triggering receptor expressed on myeloid cells 2 (*Trem2*), and COP1 E3 ubiquitin ligase (*Cop1*) as master regulators of the molecular network by *Sepp1* silencing (Figure 4D). However, only *Npc1* and *Trem2* showed reduced expression induced by at least two *Sepp1*-shRNA clones confirmed in our dataset (Figure 4E). Interestingly, *Npc1* seems to be an upstream regulator of *Apoe*, *Trem2*, and *Lamp1*, as predicted by IPA. These data suggest that *Sepp1* silencing impacts several lipid-related pathways with alterations in levels of lipid binding lipoproteins and intracellular lipid trafficking. These effects may be downstream mechanisms of reduction in EV biogenesis and secretion or may directly affect EV pathways.

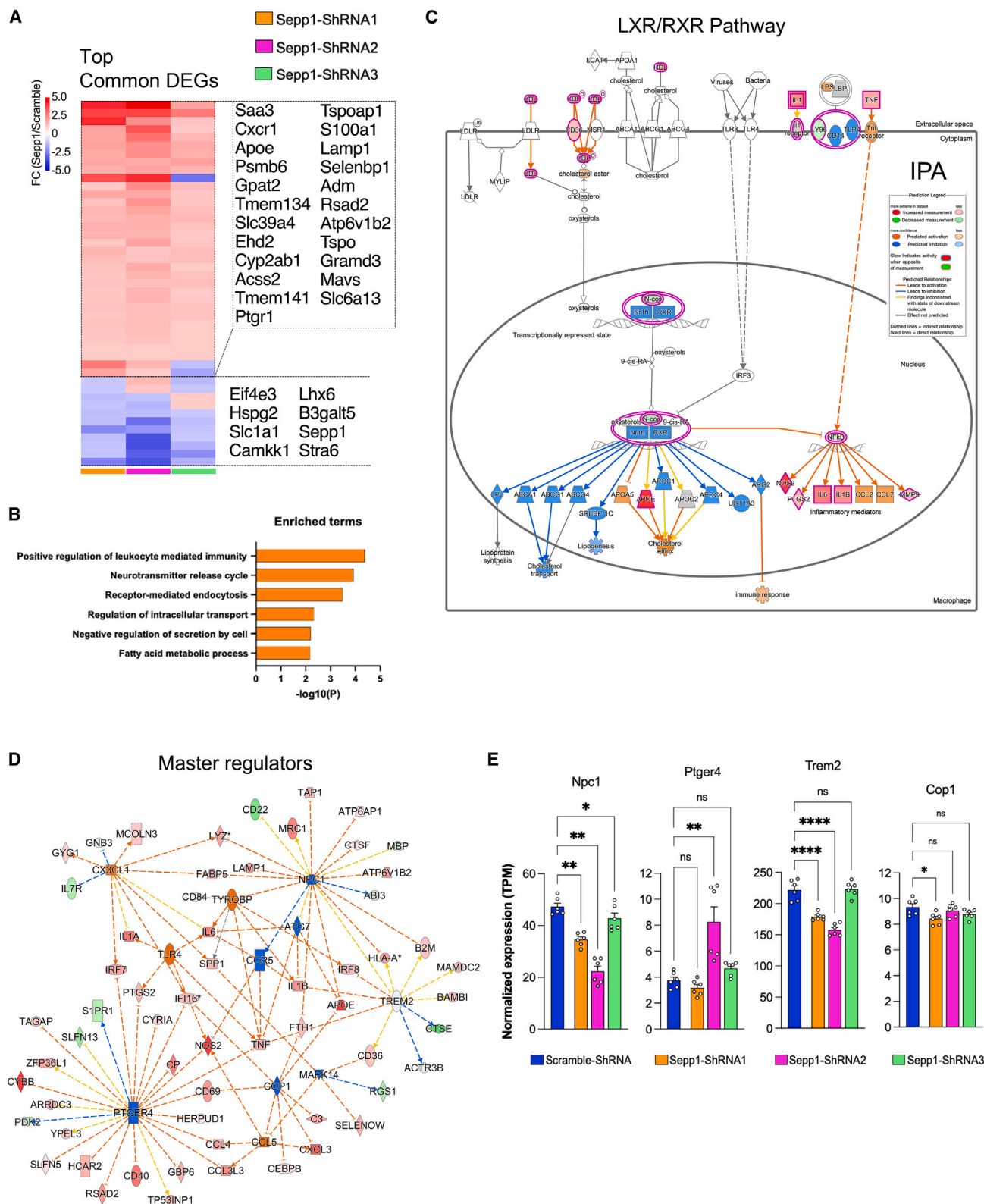
### *Sepp1* deficiency leads to increased lipid accumulation and lysosomal activity in microglia

We further validate our transcriptomic findings by RT-qPCR and immunocytochemistry, which confirmed regulation of the ESCRT-associated genes *Hgs* and *Vps37b*, the lysosomal gene *Lamp1*, and *Apoe* (Figures S5A and S5B). To validate whether transcriptomic alteration by *Sepp1* silencing reflects in functional changes in microglia, we next examined the effects of *Sepp1*-shRNA on lipid accumulation. BV-2 microglia cells were incubated with the fluorescent lipophilic dye Lipi-Deep Red for lipid staining, and intracellular lipid accumulation was live imaged over 6 h using Incucyte. Lipid accumulation in microglia was increased by all *Sepp1*-shRNAs (Figures 5A–5C). This increased lipid burden was strikingly inversely correlated with *Npc1* but not with *Apoe* expression (Figure 5D). To further confirm the *Sepp1* silencing effects on lysosomal activity, we incubated BV-2 microglia with the fluorescent dye LysoTracker for lysosomal staining. As increased numbers of lysosomes or lysosomal compartment size can be indicators of lysosome biogenesis,<sup>31</sup> we quantified the fluorescence intensity of LysoTracker over 6 h. While all *Sepp1*-shRNA clones displayed increased

#### Figure 2. Transcriptomics analysis of the effect of *Sepp1* silencing on BV-2 microglia

- (A) Principal-component analysis of transcriptomic profile of tdTomato-CD63<sup>+</sup> BV-2 cells transduced with tGFP-shRNA targeting scramble and *Sepp1* (three different clones) ( $n = 6$  replicates per group).  
(B) Heatmap displaying the Pearson correlation of scramble and *Sepp1*-shRNA replicates from RNA sequencing (RNA-seq).  
(C–E) Volcano plots comparing the DEGs of three *Sepp1*-shRNA clones versus scramble. Dashed lines indicate a significant threshold using  $q < 0.05$  ( $-\log_{10} q\text{-value} > 1.3$ ) on the y axis and  $\log_2$  fold change  $> +0.5$  or  $< -0.5$  on the x axis.  
(F) Venn diagram comparison of up- and downregulated DEGs across different *Sepp1*-shRNAs clones using the same criteria as in (D) and (E) ( $q < 0.05$  and  $\log_2$  fold change  $> +0.5$  or  $< -0.5$ ).  
(G) Common *Sepp1*-shRNA DEGs were subjected to Gene Ontology classification, and the top 5 significant ( $q < 0.05$ ) for each cellular component (CC), biological process (BP), and molecular function (MF) are displayed as a bar graph based on gene count enrichment.





(legend on next page)



LysoTracker fluorescence, *Sepp1*-shRNA2 and -shRNA3 significantly increased LysoTracker intensity (Figures 5E–5G). This increase was strongly correlated with the expression of the lysosomal marker *Lamp1* (Figure 5H). Taken together, these experiments functionally validated the transcriptomic findings of the effect of *Sepp1* silencing in BV-2 microglia, showing increased lipid accumulation and lysosomal biogenesis in response to *Sepp1* downregulation.

### ***Sepp1* silencing affects astrocytes but not neuronal EV secretion**

To investigate *Sepp1* effects in other neural cell types, we examined the effect of *Sepp1* silencing on EV secretion from primary cultured neurons and astrocytes. To achieve this goal, we transduced primary neurons at 10 days *in vitro* (DIV10) and primary astrocytes at DIV11 using a silencing RNA pool (small interfering RNA [siRNA]) targeting *Sepp1* and incubated the cells for 48 h before harvesting the CM and cell pellet (Figure 6A). We successfully achieved *Sepp1* mRNA knockdown in both neurons and astrocytes, as observed by RT-qPCR (Figures 6B and 6C); however, no change in neuronal EV secretion was observed (Figure 6D). Interestingly, primary astrocytes showed reduced EV secretion after *Sepp1* silencing (Figure 6E). These findings highlight a specific effect of *Sepp1* in regulation of EV secretion by glial cells but not by neurons, which may involve different mechanisms.

### ***Sepp1* silencing reduces EV secretion from MGnD microglia in *APP<sup>NL-G-F</sup>* mice**

Our previous work demonstrated that microglia can phagocytose, load, and secrete tau protein in EVs, contributing to the spread of tau pathology in mouse brains.<sup>21</sup> This process is exacerbated by MGnD microglia, which co-localize with A $\beta$  plaques and exhibit high levels of galectin-3 (Mac2).<sup>9</sup> Notably, MGnD/DAM microglia upregulate various common EV markers, including *Cd63* and *Cd9*.<sup>7,32,33</sup> While CD63 is associated with endo-lysosomal compartments,<sup>34</sup> CD9 is predominantly located at the plasma membrane and is secreted at higher levels compared with CD63,<sup>35</sup> making CD9<sup>+</sup> EVs a useful tool for tracking EV secretion. Given that our CD63-tdTomato lentivirus construct was not intended for microglia-specific expression, we utilized a microglia-specific lentivirus expressing mEmerald fused to CD9 (mEm-CD9)<sup>9</sup> with a miR-9 targeting sequence in the 3' UTR to monitor microglia-specific EV secretion *in vivo*.<sup>36</sup> To characterize the mEm-CD9-positive EVs secreted from microglia, we first infected BV-2 microglia with the mEm-CD9 lentivirus and isolated mEm-CD9-expressing microglia by FACS (Figure S6A); the confocal microscopy image showed CD9 positivity along the plasma membrane and tunneling nanotubes like structures protruding to neighboring cells (Figure S6B). Live im-

ages of secretion of mEm-CD9<sup>+</sup> EVs in CM (Video S1) after ATP stimulation were captured by a Leica SP8 Lightning confocal microscope. Both nanoflow cytometry and single-molecule super-resolution analysis of mEm-CD9<sup>+</sup> EVs showed a similar size distribution frequency of particles in the 50- to 125-nm-diameter size range (Figures S6C–S6G). We transduced mEm-CD9<sup>+</sup> cells with lentiviral particles for expression of mCherry-shRNA targeting *Sepp1* and observed a knockdown efficiency of ~30% (Figure S6H), which achieved a reduction of mEm-CD9<sup>+</sup> EVs secreted from cells (Figure S6I).

To assess the effect of *Sepp1* silencing in EV secretion from MGnD microglia *in vivo*, we sequentially injected a lentivirus for expression of mEm-CD9 and mCherry-shRNA targeting *Sepp1* in the hippocampus brain region of 6-month-old *APP<sup>NL-G-F</sup>* mice (Figures 7A and 7B). Approximately 85% of mEm-CD9<sup>+</sup> cells are also P2ry12<sup>+</sup> (Figures 7C and 7D), demonstrating the specificity of its expression in microglia. To quantify microglial EV secretion by MGnD microglia *in situ* in the *APP<sup>NL-G-F</sup>* mouse brain, we performed z stack reconstruction imaging of mEm-CD9<sup>+</sup>/Mac2<sup>+</sup>/mCherry<sup>+</sup> triple-positive microglia using super-resolution confocal microscopy. Three dimensional images were processed using Imaris software for automatic quantification of mEm-CD9<sup>+</sup> particles surrounding microglia (Figure 7E; Video S2). *Sepp1*-shRNA expression did not affect the Mac2 intensity in microglia from *APP<sup>NL-G-F</sup>* compared to scramble-shRNA (Figure 7F). Deconvolution of mEm-CD9<sup>+</sup> particle volume ( $\mu\text{m}^3$ ) to measure the diameter (nm) showed that *Sepp1* silencing did not impact the size distribution of mEm-CD9 particles from microglia (Figures 7G and 7H) but globally reduced the total numbers of small and large mEm-CD9<sup>+</sup> voxels per microglia (Figures 7I–7K). These findings highlight that silencing of *Sepp1* efficiently reduces EV secretion from MGnD microglia *in vivo* without changing expression level of Mac2, validating the effect of *Sepp1* on BV-2 microglia.

## **DISCUSSION**

In this study, we revealed the effects of *Sepp1* silencing, which has a direct impact on biogenesis and secretion of EVs by glial cells *in vitro* and in MGnD microglia bearing A $\beta$  plaques in *APP<sup>NL-G-F</sup>* mice. We used two recently developed lentiviral EV fluorescent reporters, tdTomato-CD63 and mEmerald-CD9, to access the EV secretion and membrane sorting of tetraspanin in EVs by microglia in response to regulation of *Sepp1*. These methods allowed the visualization and quantification of CD63 single molecules loaded on EVs, which also refers to the endosome origin of EVs secreted by microglia, and *in vivo* specific labeling of microglia EVs with mEm-CD9 for unbiased quantification of CD9<sup>+</sup> particles as an indirect method to assess microglia EV secretion *in situ*.

**Figure 4. *Sepp1* silencing affects the lipid metabolism and inter/intracellular trafficking**

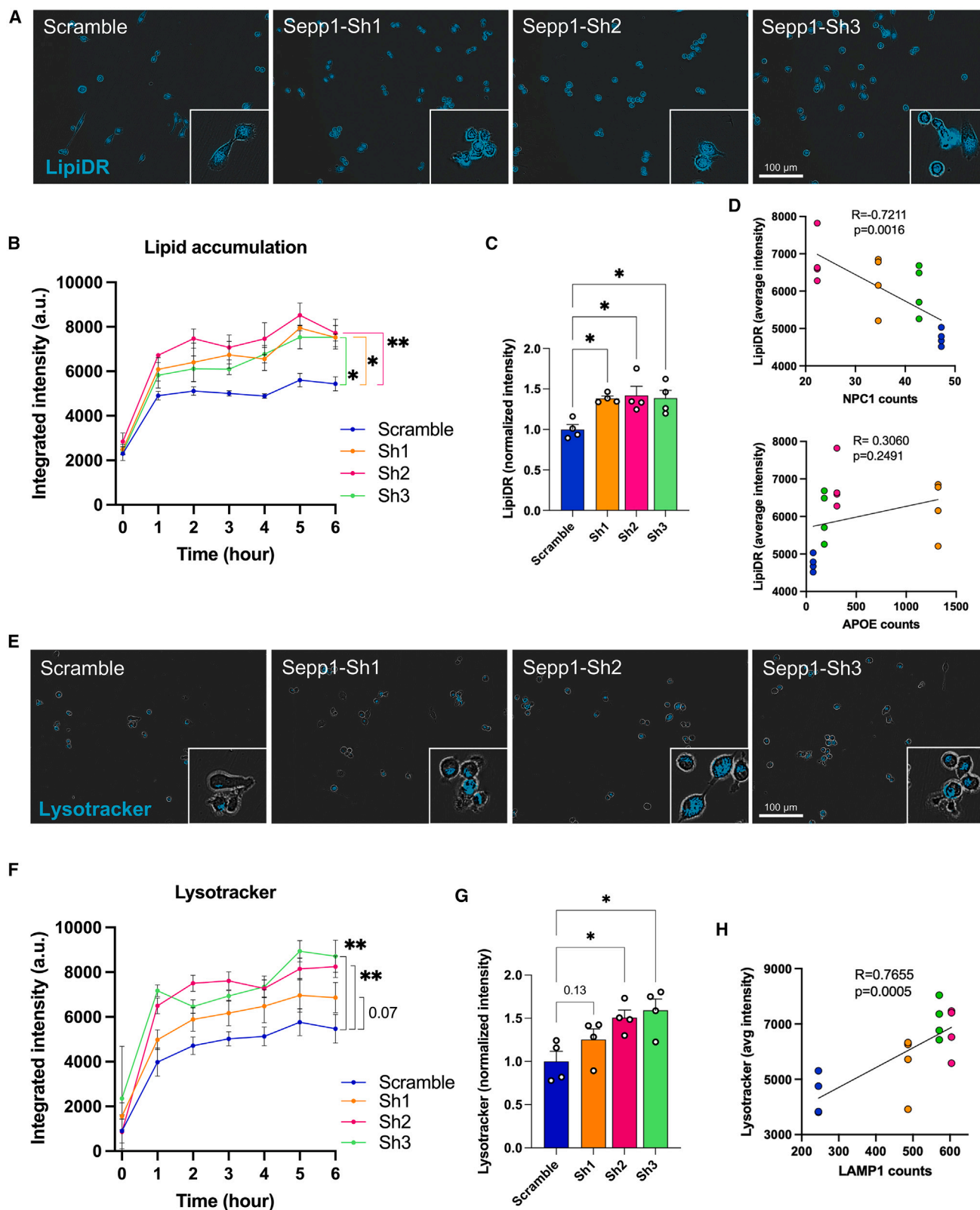
(A) Heatmap displaying the top common DEGs ( $q < 0.05$ ) regulated in response to *Sepp1* downregulation.

(B) Enriched pathways associated with the common DEGs in *Sepp1*-shRNA were obtained using Metascape software.

(C and D) Ingenuity Pathway Analysis (IPA) using all common DEGs regulated in different *Sepp1*-shRNA groups predicted LXR/RXR pathway downregulation and identified a network interaction composed mainly of *Ptger4*, *Npc1*, *Trem2*, and *Cop1* in response to *Sepp1* downregulation (D).

(E) Analysis of normalized expression of *Ptger4*, *Npc1*, *Trem2*, and *Cop1* in RNA-seq data. \* $p < 0.05$ , \*\* $p < 0.01$ , and \*\*\*\* $p < 0.0001$  by one-way ANOVA with Holm-Sidak post hoc analysis ( $n = 6$  replicates per group). Bar graphs indicate mean  $\pm$  SEM.





(legend on next page)

EV cargo composition reflects host cell content and could be dynamically altered in response to stimuli. ATP has been shown to trigger EV secretion from macrophages and microglia through activation of purinergic receptors, including purinergic receptor 7 (P2RX7).<sup>37,38</sup> P2RX7 expression levels are increased in the brain tissue of patients with AD and AD animal models and especially correlate with microglial cells surrounding A $\beta$  plaques.<sup>39,40</sup> Our group recently described that A $\beta$  plaque-associated Mac2<sup>+</sup> MGnD microglia display increased Tsg101 immunoreactivity and secretion of mEm-CD9<sup>+</sup> EVs compared to homeostatic microglia (Mac2<sup>-</sup>), indicating increased EV biogenesis in MGnD microglia in *APP<sup>NL-G-F</sup>* mice. Additionally, p-tau levels are increased in MGnD microglia-specific mEm-CD9<sup>+</sup> EVs, and microglia depletion using a colony-stimulating factor 1 receptor inhibitor (PLX5622) reduces the propagation of p-tau in the brains of wild-type and *APP<sup>NL-G-F</sup>* mice expressing P301L mutant tau.<sup>9,21</sup> These pieces of evidence suggest that disease-associated microglia may play a role in AD progression through increased production of EVs and exacerbated EV secretion in response to ATP-mediated P2RX7 activation. Strikingly, this study shows that *Sepp1* silencing can strongly reduce EV secretion by both ATP-stimulated microglia *in vitro* and MGnD microglia *in vivo*, demonstrating *Sepp1* as a promising target to regulate EV secretion from microglia.

A previous study from our group showed that *Sepp1* silencing did not affect the increased IL-1 $\beta$  expression in primary microglia in response to LPS and ATP stimulation. However, *Sepp1* silencing decreased the IL-1 $\beta$  protein levels associated with the microglia EV fraction.<sup>22</sup> In the current study, we found that not only EV secretion but also loading of tetraspanin CD63 on EVs were decreased, as well as CD63 expression in microglia, indicating an effect of *Sepp1* in exosomes, as CD63 has an endosomal origin and is enriched in exosome-sized EVs.<sup>34,41</sup> These effects might be explained by reduced EV biogenesis or EV cargo loading because of downregulation of the ESCRT machinery (*Vps4b*, *Alix*, *Hgs*, and *Vps37b*) induced by *Sepp1* silencing. EVs can form by budding of the plasma membrane or by an intracellular endocytic pathway involving the fusion of multivesicular bodies (MVBs) originating from late endosome compartments, resulting in extracellular release of intraluminal vesicles (ILVs).<sup>10,42</sup> The ESCRT system consists of a family of protein complexes (ESCRT-0, -I, -II, and -III) that play a role at the membrane of MVBs to regulate dynamic membrane processes involved in biogenesis and cargo sorting into ILVs. Impairment of the ESCRT machinery by *Sepp1* silencing may culminate in disruption

of ESCRT complexes and disturb EV production, cargo sorting, and trafficking in microglia. In addition, a recent study has shown that inhibition of endocytosis by either inhibitors or expression of the exosome biogenesis factor syntenin can increase the vesicular secretion of exosomal tetraspanins in small vesicles<sup>43</sup>; therefore, regulation of endocytosis by *Sepp1* silencing may also impact EV secretion in microglia. Indeed, our previous genome-wide shRNA library screening using BV-2 microglia identified that silencing of the EV biogenesis-associated molecules *Sdc1*, *Vps4a*, and *Hgs* was as effective as silencing *Sepp1* to reduce EV secretion from BV-2 microglia. However, silencing *Sdc1* and *Vps4a* did not affect ATP-induced EV secretion, and significant toxicity was observed after silencing *Hgs* in BV-2 microglia.<sup>22</sup> This led us to focus on non-ESCRT molecules, such as *Sepp1*, for regulating EV secretion from microglia.

*Sepp1* protein can bind to heparin sulfate proteoglycans (HSPGs) on the cell membrane surface through two histidine-enriched sequences on its N-terminal domain, which can promote uptake by cells.<sup>44,45</sup> *Sepp1* also binds to apolipoprotein E receptor 2, a member of the lipoprotein receptor family, using the clathrin-dependent endocytosis pathway and mediates delivery of selenium from hepatocytes to the brain.<sup>46</sup> Intriguingly, *Sepp1* is loaded in exosomes secreted from hepatocytes that can deliver *Sepp1* to endothelial and neuronal cells. This EV loading of *Sepp1* is negatively regulated by interaction with ApoE in a process mediated by heparin-binding sites of *Sepp1*.<sup>28</sup> Here, we observed evidence of causal regulation of ApoE transcript levels by *Sepp1* silencing. Another interesting fact is the interaction of both *Sepp1* and EVs with HSPGs, which also plays a role in vesicle formation and trafficking<sup>47</sup> and has been reported as a mediator for EV internalization in different cell lines.<sup>48,49</sup> Despite the established role of *Sepp1* in selenium metabolism, no physiological role in microglia has been reported. In addition to the regulation of EV biogenesis, we found that *Sepp1* can also regulate several components of intracellular machinery in microglia, including genes involved in lipid metabolism and lysosomal pathways, such as the lysosomal protein *Lamp1*, resulting in an increased accumulation of lipids and biogenesis of lysosomes. Whether this effect is an indirect or direct consequence of reduced EV secretion and redistribution of intracellular lipids for clearance through lysosomal compartments needs to be investigated further. Beyond the role in intercellular communication under physiological conditions, EVs can also play a role in removing undesired and toxic cellular contents, such as A $\beta$  and tau aggregates, through secretion into the extracellular space.<sup>19,20</sup> As an

#### Figure 5. *Sepp1* regulates lipid efflux and lysosomal activity in microglia

- (A) BV-2 microglia cells were incubated with Lipi-Deep Red (LipiDR) for neutral lipid staining, and live images were acquired every 1 h for 6 h using Incucyte. Shown are representative images of LipiDR accumulation in BV-2 microglia cells. Scale bar, 100  $\mu$ m.
- (B) Quantification of LipiDR intensity over 6 h of incubation ( $n = 4$  replicates per group). \* $p < 0.05$  and \*\* $p < 0.01$  by repeated-measures two-way ANOVA with Holm-Sidak post hoc analysis.
- (C) Normalized intensity of LipiDR after 6 h of incubation ( $n = 4$  replicates per group). \* $p < 0.05$  by one-way ANOVA with Holm-Sidak post hoc analysis.
- (D) Correlation analysis of LipiDR intensity with average values of *Npc1* and *ApoE* transcript levels.
- (E) BV-2 microglia cells were incubated with LysoTracker for staining of lysosomal compartments, and live images were acquired every 1 h for 6 h using Incucyte. Shown are representative images of LysoTracker in cells. Scale bar, 100  $\mu$ m.
- (F) Quantification of LysoTracker intensity over 6 h of incubation ( $n = 4$  replicates per group). \*\* $p < 0.01$  by repeated-measures two-way ANOVA with Holm-Sidak post hoc analysis.
- (G) Normalized intensity of LysoTracker after 6 h of incubation ( $n = 4$  replicates per group). \* $p < 0.05$  by one-way ANOVA with Holm-Sidak post hoc analysis.
- (H) Correlation analysis of LysoTracker intensity with average values of *Lamp1* transcripts levels. Graphs indicate mean  $\pm$  SEM.

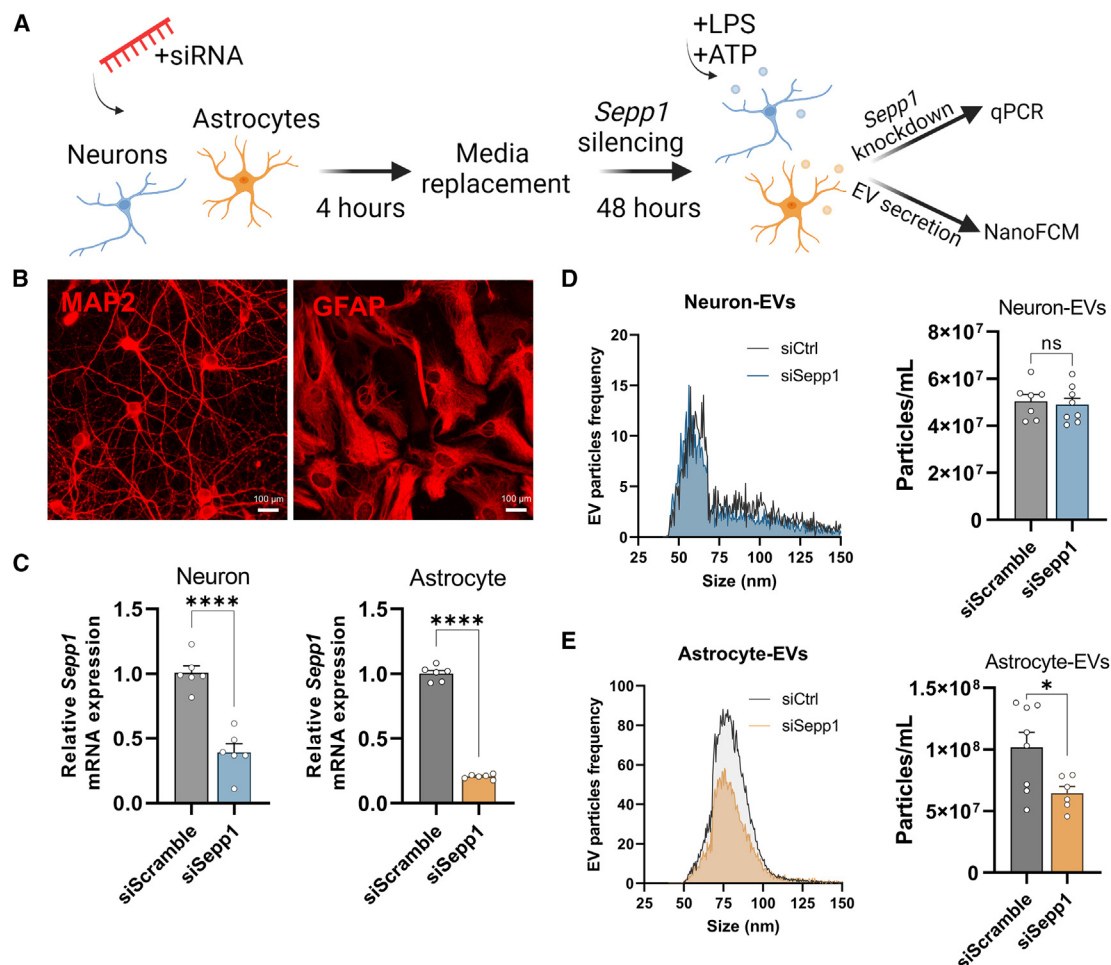


**Figure 6. *Sepp1* silencing effects on neuronal and astrocytic EV secretion**

(A) Schematic of the experimental design for *Sepp1* silencing using siRNA in primary neurons and primary astrocytes.

(B) Representative MAP2 and GFAP immunostaining images in primary neurons and astrocytes. Scale bar, 100  $\mu$ m.

(C) Bar graphs showing relative expression of *Sepp1* mRNA in primary neurons and astrocytes treated with siRNA targeting the scramble control sequence or *Sepp1* ( $n = 6$  replicates per group from 2 independent experiments). \*\*\*\* $p < 0.0001$  by two-tailed student t test.

(D and E) Size distribution and concentration of EVs secreted in CM of primary neurons (D) and astrocytes (E) measured by nanoflow cytometry (NanoFCM) ( $n = 6$ –8 replicates per group from 2 independent experiments). \* $p < 0.05$  by two-tailed student t-test; ns, no significance. Data are represented as mean  $\pm$  SEM.

alternative pathway of EV secretion, MVBs can also fuse with lysosomes directing ILV content to degradation.<sup>50</sup> The mechanism of deciding whether MVBs will be directed to the plasma membrane or to the lysosomes is not well understood. It is possible that EVs might serve as an alternative disposal pathway to counteract overloaded lysosomal machinery,<sup>51</sup> and previous studies have reported that inhibition of lysosomal activity increases the loading of  $\alpha$ -synuclein in EVs released by the SH-SY5Y neuroblastoma cell line.<sup>52</sup> In this sense, downregulation of EV biogenesis and secretion may re-route intracellular products to lysosomal compartments in microglia, stimulating increased lysosomal activity to balance cellular waste clearance and compensate for reduced EV secretion.

We further showed that *Sepp1* had a predominant effect on glial EV secretion but did not change neuronal EV secretion. This dif-

ferential regulation in glial cells might be explained by microglia and astrocytes being key regulators of inflammatory responses in the CNS and highly responsive to ATP, a molecule that is present in neuroinflammation.<sup>53</sup> Interestingly, EVs secreted by activated astrocytes are also known to contribute to the inflammatory response and neuronal function and correlate with the proteome of EVs isolated from the postmortem brain tissue of patients with AD brains.<sup>54,55</sup> Overall, *Sepp1* can be a good candidate for regulation of pathological EV secretion from glial cells, and future studies should uncover how *Sepp1* regulation in these cells may affect neuronal function.

#### Limitations of the study

In this study, we used the BV-2 cell line for studying *Sepp1* silencing effects, as we previously validated similar effects of

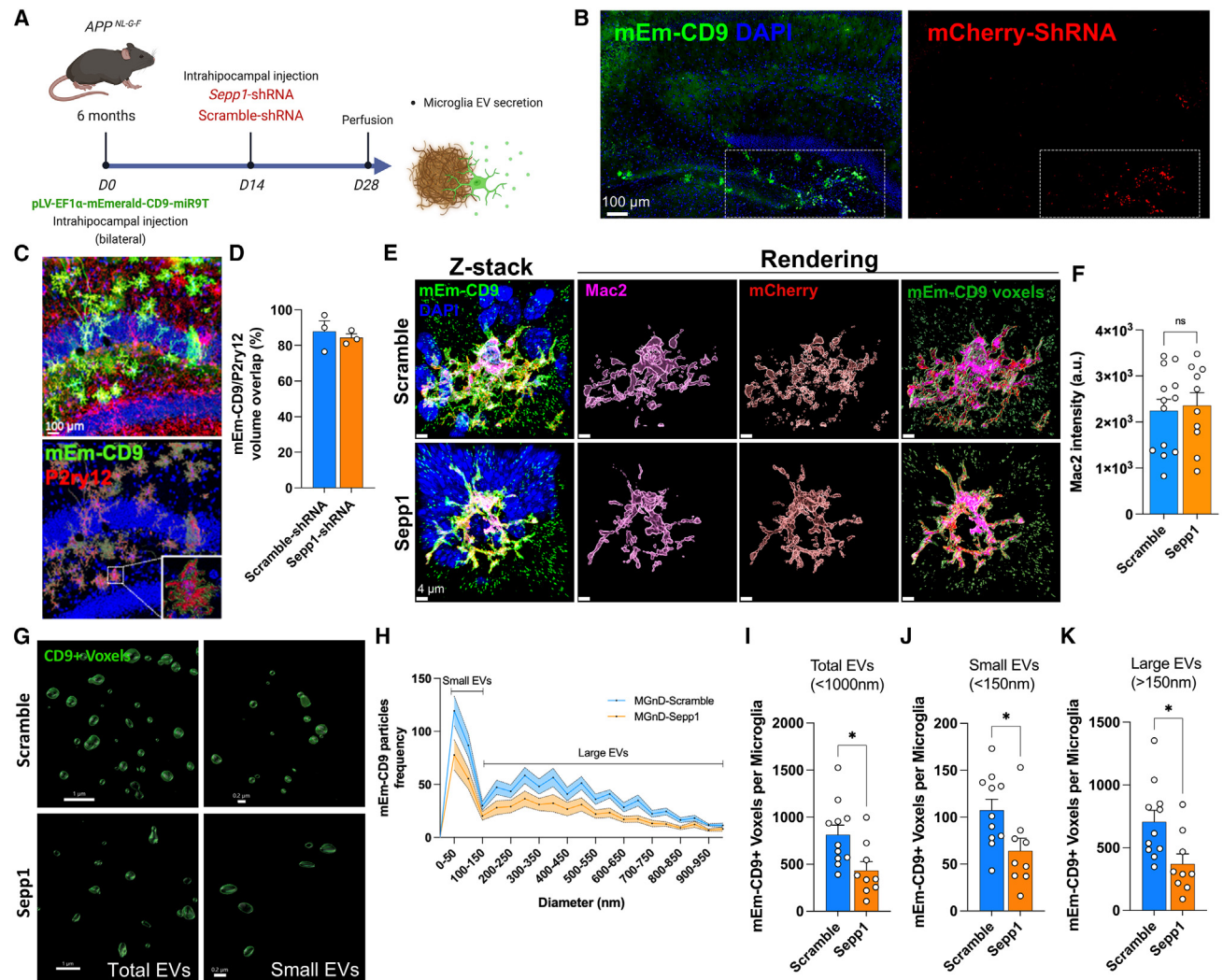


**Figure 7. *Sepp1* silencing downregulates EV secretion from MGnD microglia in *APP<sup>NL-G-F</sup>* mice**

(A) Experimental design for microglia-specific EV labeling and *Sepp1* silencing in *APP<sup>NL-G-F</sup>* mice. Six-month-old mice received injections into the hippocampus with a lentivirus for microglia-specific expression of mEm-CD9, followed by a lentivirus injection for scramble-shRNA:mCherry or *Sepp1*-shRNA:mCherry expression 2 weeks later.

(B) Representative images of mEm-CD9<sup>+</sup> (green) microglia cells and cells expressing mCherry:shRNA (red) in the *APP<sup>NL-G-F</sup>* mouse dentate gyrus in the hippocampus brain region. Scale bar, 100  $\mu$ m.

(C) Confocal microscopy and Imaris 3D rendering of mouse hippocampal tissue. Shown are mEm-CD9<sup>+</sup> (green) and P2ry12<sup>+</sup> (red). Scale bar, 100  $\mu$ m.

(D) Percentage of the P2ry12 marker overlapped with mEm-CD9<sup>+</sup> cells in the hippocampus of *APP<sup>NL-G-F</sup>* mice injected with shRNA.

(E) Super-resolution confocal z stack images of single microglia co-transduced with mEm-CD9 and shRNA:mCherry in the hippocampus of *APP<sup>NL-G-F</sup>* mice. 3D images of shRNA:mCherry (red) and Mac2 (magenta) surfaces overlapped with mEm-CD9<sup>+</sup> (green) microglia as well as mEm-CD9<sup>+</sup> particles surrounding microglia were generated using Imaris software. Scale bar, 4  $\mu$ m.

(F) Measured Mac2 fluorescence intensity in scramble- and *Sepp1*-shRNA-transduced microglia in *APP<sup>NL-G-F</sup>* mice ( $n = 3-4$  microglia per mouse, 3-4 mice per group). Two-tailed student t test; ns, no significance.

(G) Representative high-magnification images of mEm-CD9<sup>+</sup> voxels obtained in areas surrounding Mac2<sup>+</sup> MGnD microglia as in (E). Scale bars: total EVs, 1  $\mu$ m; small EVs, 0.2  $\mu$ m.

(H-K) *In situ* analysis of mEm-CD9<sup>+</sup> voxels surrounding mEm-CD9<sup>+</sup>/Mac2<sup>+</sup> MGnD microglia. Shown are (H) the size frequency distribution of mEm-CD9<sup>+</sup> particles and quantification of the number of mEm-CD9<sup>+</sup> voxels per microglia in total EVs (I, total EVs <1,000 nm), small EVs (J, <150 nm), and large EVs (K, >150 nm) among scramble- and *Sepp1*-shRNA-transduced mEm-CD9<sup>+</sup>/Mac2<sup>+</sup> MGnD microglia. Two-tailed student t test, \* $p < 0.05$  ( $n = 3-4$  microglia per mouse, 3-4 mice per group). Data are represented as mean  $\pm$  SEM.

*Sepp1* silencing in both BV-2 and primary microglia cell EV secretion. While this cell line represents a valuable tool for microglia studies and makes possible the generation of stable

EV reporter cell lines, it displays differences that should be considered regarding its morphology, adhesion, and higher proliferation compared to primary microglial cells and potentially



differentiates these cells from microglia *in vivo*. We also acknowledge that shRNA technology would have on and off-target effects, which was assessed in our study by comparing different shRNA clones. We approached our bulk RNA sequencing analysis by targeting only differential expressed genes that were found to be regulated by at least two *Sepp1*-shRNA clones. Using this strategy, we could minimize the potential confounding off-target effects by each clone and focus on genes that were commonly regulated by *Sepp1* silencing.

We previously observed that LPS and ATP induction stimulates the microglial release of small EVs ranging from 30 to 220 nm by nanoparticle tracking analysis using Nanosight.<sup>22</sup> Here, we applied a recently developed nanoflow cytometry technique using a flow nanoanalyzer (NanoFCM), which relies on different calibrations for small (~68–155 nm) and large (~155–850 nm) particles, providing separate measurements for small and large EV concentrations and size distributions. While Nanosight provides a broad range of EV size distributions from ~10–1000 nm, we observed that the flow nanoanalyzer provides lower counts at the extremes, particularly at the maximum particle size, which may be explained by high enrichment of small EVs in our samples or might represent a technical limiting factor that should be considered when measuring particles at the limits of a standard curve.

## Conclusions

In summary, we show that *Sepp1* silencing impacts microglia EV biogenesis and secretion, which can efficiently reduce EV secretion from MGNd microglia *in vivo* in AD mouse models. Silencing of *Sepp1* also regulated lipid accumulation and lysosomal proliferation in microglia. Specifically targeting *Sepp1* in microglia may represent a potential approach to reduce microglia spread of pathological signals through EVs and may have a potential application that can be further explored in neurodegenerative diseases such as AD.

## RESOURCE AVAILABILITY

### Lead contact

Requests for any additional information and reagents should be directed to and will be fulfilled by the lead contact, Tsuneya Ikezu ([ikezu.tsuneya@mayo.edu](mailto:ikezu.tsuneya@mayo.edu)).

### Materials availability

Reagents used in this study are publicly available or available from the [lead contact](#) upon request.

### Data and code availability

- Bulk RNA sequencing data generated in this study have been deposited at the Sequence Read Archive/BioProject and are publicly available under accession number: PRJNA1179490 (<https://www.ncbi.nlm.nih.gov/bioproject/?term=PRJNA1179490>).
- This paper does not report original code.
- Any additional information required to re-analyze data reported in this paper is available from the [lead contact](#) upon request.

## ACKNOWLEDGMENTS

We would like to thank all current and former members of the Laboratory of Molecular NeuroTherapeutics, including Katrina R.G. Bueser, Dr. Zhengrong Zhang, and Dr. Grace Samtani for technical assistance and Dr. Yang You for

bioinformatic analysis support. We would also like to thank Dr. Laura J. Lewis-Tuffin and Margaret L. Ushman at the MCF Cytometry and Imaging Laboratory at the Mayo Clinic Florida and Dr. Jiaming Guo from ONI. This work was funded in part by NIH RF1 AG054199 (to T.I.), R01 AG054672 (to T.I.), R01 AG066429 (to T.I.), R01 AG067763 (to T.I.), R01 AG072719 (to T.I.), RF1 AG082704 (to T.I. and S.I.), R01 AG079859 (to S.I.), and Cure Alzheimer's Fund (to T.I. and S.I.).

## AUTHOR CONTRIBUTIONS

Conceptualization, V.B.-S. and T.I.; methodology, V.B.-S. and Z.R.; investigation, V.B.-S., Z.R., B.C.M., and I.P.; formal analysis, V.B.-S. and B.C.M.; bioinformatics and visualization, V.B.-S.; manuscript writing and editing, V.B.-S., B.C.M., S.I., and T.I. All authors have read and approved the final version of the manuscript.

## DECLARATION OF INTERESTS

The authors declare no competing interests.

## STAR★METHODS

Detailed methods are provided in the online version of this paper and include the following:

- **KEY RESOURCES TABLE**
- **EXPERIMENTAL MODEL AND STUDY PARTICIPANT DETAILS**
  - Ethical approval and consent to participate
  - Animals and genotyping
  - Cell lines
- **METHOD DETAILS**
  - Lentiviral vector construction
  - Establishment of EV reporter BV-2 cell lines
  - Lentivirus transduction of shRNA
  - Isolation of the EV-enriched fraction
  - Nano-flow cytometry (NanoFCM)
  - Single molecule super-resolution microscopy
  - Confocal live imaging
  - Stereotaxic surgery
  - Histological processing and immunofluorescence staining
  - RNA isolation and bulk RNA sequencing
  - Bioinformatic and pathway analysis
  - Live imaging of cell phagocytosis, lipid accumulation and lysosome monitoring
  - Primary cell culture
  - qRT-PCR analysis
  - Immunocytochemistry (ICC)
- **QUANTIFICATION AND STATISTICAL ANALYSIS**

## SUPPLEMENTAL INFORMATION

Supplemental information can be found online at <https://doi.org/10.1016/j.celrep.2024.115025>.

Received: April 14, 2024

Revised: September 22, 2024

Accepted: November 12, 2024

Published: November 30, 2024

## REFERENCES

1. Salter, M.W., and Stevens, B. (2017). Microglia emerge as central players in brain disease. *Nat. Med.* 23, 1018–1027. <https://doi.org/10.1038/nm.4397>.
2. Ousman, S.S., and Kubes, P. (2012). Immune surveillance in the central nervous system. *Nat. Neurosci.* 15, 1096–1101. <https://doi.org/10.1038/nn.3161>.



3. Solé-Domènech, S., Cruz, D.L., Capetillo-Zarate, E., and Maxfield, F.R. (2016). The endocytic pathway in microglia during health, aging and Alzheimer's disease. *Ageing Res. Rev.* 32, 89–103. <https://doi.org/10.1016/j.arr.2016.07.002>.
4. Heneka, M.T., Carson, M.J., El Khoury, J., Landreth, G.E., Brosseron, F., Feinstein, D.L., Jacobs, A.H., Wyss-Coray, T., Vitorica, J., Ransohoff, R.M., et al. (2015). Neuroinflammation in Alzheimer's disease. *Lancet Neurol.* 14, 388–405. [https://doi.org/10.1016/S1474-4422\(15\)70016-5](https://doi.org/10.1016/S1474-4422(15)70016-5).
5. Leng, F., and Edison, P. (2021). Neuroinflammation and microglial activation in Alzheimer disease: where do we go from here? *Nat. Rev. Neurol.* 17, 157–172. <https://doi.org/10.1038/s41582-020-00435-y>.
6. Krasemann, S., Madore, C., Cialic, R., Baufeld, C., Calcagno, N., El Fattimy, R., Beckers, L., O'Loughlin, E., Xu, Y., Fanek, Z., et al. (2017). The TREM2-APOE Pathway Drives the Transcriptional Phenotype of Dysfunctional Microglia in Neurodegenerative Diseases. *Immunity* 47, 566–581.e9. <https://doi.org/10.1016/j.immuni.2017.08.008>.
7. Deczkowska, A., Keren-Shaul, H., Weiner, A., Colonna, M., Schwartz, M., and Amit, I. (2018). Disease-Associated Microglia: A Universal Immune Sensor of Neurodegeneration. *Cell* 173, 1073–1081. <https://doi.org/10.1016/j.cell.2018.05.003>.
8. Clayton, K.A., Van Eno, A.A., and Ikezu, T. (2017). Alzheimer's Disease: The Role of Microglia in Brain Homeostasis and Proteopathy. *Front. Neurosci.* 11, 680. <https://doi.org/10.3389/fnins.2017.00680>.
9. Clayton, K., Delpech, J.C., Herron, S., Iwahara, N., Ericsson, M., Saito, T., Saido, T.C., Ikezu, S., and Ikezu, T. (2021). Plaque associated microglia hyper-secrete extracellular vesicles and accelerate tau propagation in a humanized APP mouse model. *Mol. Neurodegener.* 16, 18. <https://doi.org/10.1186/s13024-021-00440-9>.
10. van Niel, G., D'Angelo, G., and Raposo, G. (2018). Shedding light on the cell biology of extracellular vesicles. *Nat. Rev. Mol. Cell Biol.* 19, 213–228. <https://doi.org/10.1038/nrm.2017.125>.
11. Yáñez-Mó, M., Siljander, P.R., Andreu, Z., Zavec, A.B., Borrás, F.E., Buzas, E.I., Buzas, K., Casal, E., Cappello, F., Carvalho, J., et al. (2015). Biological properties of extracellular vesicles and their physiological functions. *J. Extracell. Vesicles* 4, 27066. <https://doi.org/10.3402/jev.v4.27066>.
12. Delpech, J.C., Herron, S., Botros, M.B., and Ikezu, T. (2019). Neuroimmune Crosstalk through Extracellular Vesicles in Health and Disease. *Trends Neurosci.* 42, 361–372. <https://doi.org/10.1016/j.tins.2019.02.007>.
13. You, Y., and Ikezu, T. (2019). Emerging roles of extracellular vesicles in neurodegenerative disorders. *Neurobiol. Dis.* 130, 104512. <https://doi.org/10.1016/j.nbd.2019.104512>.
14. Burnstock, G. (2007). Physiology and pathophysiology of purinergic neurotransmission. *Physiol. Rev.* 87, 659–797. <https://doi.org/10.1152/physrev.00043.2006>.
15. Drago, F., Lombardi, M., Prada, I., Gabrielli, M., Joshi, P., Cojoc, D., Franck, J., Fournier, I., Vizioli, J., and Verderio, C. (2017). ATP Modifies the Proteome of Extracellular Vesicles Released by Microglia and Influences Their Action on Astrocytes. *Front. Pharmacol.* 8, 910. <https://doi.org/10.3389/fphar.2017.00910>.
16. Kumar, A., Stoica, B.A., Loane, D.J., Yang, M., Abulwerdi, G., Khan, N., Kumar, A., Thom, S.R., and Faden, A.I. (2017). Microglial-derived microparticles mediate neuroinflammation after traumatic brain injury. *J. Neuroinflammation* 14, 47. <https://doi.org/10.1186/s12974-017-0819-4>.
17. Verderio, C., Muzio, L., Turola, E., Bergami, A., Novellino, L., Ruffini, F., Riganti, L., Corradini, I., Francolini, M., Garzetti, L., et al. (2012). Myeloid microvesicles are a marker and therapeutic target for neuroinflammation. *Ann. Neurol.* 72, 610–624. <https://doi.org/10.1002/ana.23627>.
18. Yang, Y., Boza-Serrano, A., Dunning, C.J.R., Clausen, B.H., Lambertsen, K.L., and Deierborg, T. (2018). Inflammation leads to distinct populations of extracellular vesicles from microglia. *J. Neuroinflammation* 15, 168. <https://doi.org/10.1186/s12974-018-1204-7>.
19. Ruan, Z., Pathak, D., Venkatesan Kalavai, S., Yoshii-Kitahara, A., Murakawa, S., Bhatt, N., Takamatsu-Yukawa, K., Hu, J., Wang, Y., Hersch, S., et al. (2021). Alzheimer's disease brain-derived extracellular vesicles spread tau pathology in interneurons. *Brain* 144, 288–309. <https://doi.org/10.1093/brain/awaa376>.
20. Bodart-Santos, V., Pinheiro, L.S., da Silva-Junior, A.J., Froza, R.L., Ahrens, R., Gonçalves, R.A., Andrade, M.M., Chen, Y., Alcantara, C.L., Grinberg, L.T., et al. (2023). Alzheimer's disease brain-derived extracellular vesicles reveal altered synapse-related proteome and induce cognitive impairment in mice. *Alzheimers Dement.* 19, 5418–5436. <https://doi.org/10.1002/alz.13134>.
21. Asai, H., Ikezu, S., Tsunoda, S., Medalla, M., Luebke, J., Haydar, T., Wolozin, B., Butovsky, O., Kügler, S., and Ikezu, T. (2015). Depletion of microglia and inhibition of exosome synthesis halt tau propagation. *Nat. Neurosci.* 18, 1584–1593. <https://doi.org/10.1038/nn.4132>.
22. Ruan, Z., Takamatsu-Yukawa, K., Wang, Y., Ushman, M.L., Labadorf, A.T., Ericsson, M., Ikezu, S., and Ikezu, T. (2022). Functional genome-wide short hairpin RNA library screening identifies key molecules for extracellular vesicle secretion from microglia. *Cell Rep.* 39, 110791. <https://doi.org/10.1016/j.celrep.2022.110791>.
23. Burk, R.F., and Hill, K.E. (2009). Selenoprotein P-expression, functions, and roles in mammals. *Biochim. Biophys. Acta* 1790, 1441–1447. <https://doi.org/10.1016/j.bbagen.2009.03.026>.
24. Saito, Y. (2020). Selenoprotein P as a significant regulator of pancreatic beta cell function. *J. Biochem.* 167, 119–124. <https://doi.org/10.1093/jb/mvz061>.
25. Saito, Y. (2021). Selenium Transport Mechanism via Selenoprotein P-Its Physiological Role and Related Diseases. *Front. Nutr.* 8, 685517. <https://doi.org/10.3389/fnut.2021.685517>.
26. Oo, S.M., Oo, H.K., Takayama, H., Ishii, K.A., Takeshita, Y., Goto, H., Nakano, Y., Kohno, S., Takahashi, C., Nakamura, H., et al. (2022). Selenoprotein P-mediated reductive stress impairs cold-induced thermogenesis in brown fat. *Cell Rep.* 38, 110566. <https://doi.org/10.1016/j.celrep.2022.110566>.
27. Saito, Y., and Takahashi, K. (2002). Characterization of selenoprotein P as a selenium supply protein. *Eur. J. Biochem.* 269, 5746–5751. <https://doi.org/10.1046/j.1432-1033.2002.03298.x>.
28. Jin, Y., Chung, Y.W., Jung, M.K., Lee, J.H., Ko, K.Y., Jang, J.K., Ham, M., Kang, H., Pack, C.G., Mihara, H., and Kim, I.Y. (2020). Apolipoprotein E-mediated regulation of selenoprotein P transportation via exosomes. *Cell. Mol. Life Sci.* 77, 2367–2386. <https://doi.org/10.1007/s00018-019-03287-y>.
29. Blasi, E., Barluzzi, R., Bocchini, V., Mazzolla, R., and Bistoni, F. (1990). Immortalization of murine microglial cells by a v-raf/v-myc carrying retrovirus. *J. Neuroimmunol.* 27, 229–237. [https://doi.org/10.1016/0165-5728\(90\)90073-v](https://doi.org/10.1016/0165-5728(90)90073-v).
30. Varnum, M.M., Clayton, K.A., Yoshii-Kitahara, A., Yonemoto, G., Koro, L., Ikezu, S., and Ikezu, T. (2017). A split-luciferase complementation, real-time reporting assay enables monitoring of the disease-associated transmembrane protein TREM2 in live cells. *J. Biol. Chem.* 292, 10651–10663. <https://doi.org/10.1074/jbc.M116.759159>.
31. Barral, D.C., Staiano, L., Guimas Almeida, C., Cutler, D.F., Eden, E.R., Futter, C.E., Galione, A., Marques, A.R.A., Medina, D.L., Napolitano, G., et al. (2022). Current methods to analyze lysosome morphology, positioning, motility and function. *Traffic* 23, 238–269. <https://doi.org/10.1111/tra.12839>.
32. Mancuso, R., Fattorelli, N., Martinez-Muriana, A., Davis, E., Wolfs, L., Van Den Daele, J., Geric, I., Premereur, J., Polanco, P., Bijnens, B., et al. (2024). Xenografted human microglia display diverse transcriptomic states in response to Alzheimer's disease-related amyloid-beta pathology. *Nat. Neurosci.* 27, 886–900. <https://doi.org/10.1038/s41593-024-01600-y>.
33. Keren-Shaul, H., Spinrad, A., Weiner, A., Matcovitch-Natan, O., Dvir-Sternfeld, R., Ulland, T.K., David, E., Baruch, K., Lara-Astaiso, D., Toth, B., et al. (2017). A Unique Microglia Type Associated with Restricting

- Development of Alzheimer's Disease. *Cell* 169, 1276–1290.e17. <https://doi.org/10.1016/j.cell.2017.05.018>.
34. Mathieu, M., Névo, N., Jouve, M., Valenzuela, J.I., Maurin, M., Verweij, F.J., Palmulli, R., Lankar, D., Dingli, F., Loew, D., et al. (2021). Specificities of exosome versus small ectosome secretion revealed by live intracellular tracking of CD63 and CD9. *Nat. Commun.* 12, 4389. <https://doi.org/10.1038/s41467-021-24384-2>.
35. Fordjour, F.K., Guo, C., Ai, Y., Daaboul, G.G., and Gould, S.J. (2022). A shared, stochastic pathway mediates exosome protein budding along plasma and endosome membranes. *J. Biol. Chem.* 298, 102394. <https://doi.org/10.1016/j.jbc.2022.102394>.
36. Åkerblom, M., Sachdeva, R., Quintino, L., Wettergren, E.E., Chapman, K.Z., Manfre, G., Lindvall, O., Lundberg, C., and Jakobsson, J. (2013). Visualization and genetic modification of resident brain microglia using lentiviral vectors regulated by microRNA-9. *Nat. Commun.* 4, 1770. <https://doi.org/10.1038/ncomms2801>.
37. Ruan, Z., Delpech, J.C., Venkatesan Kalavai, S., Van Enoo, A.A., Hu, J., Ikezu, S., and Ikezu, T. (2020). P2RX7 inhibitor suppresses exosome secretion and disease phenotype in P301S tau transgenic mice. *Mol. Neurodegener.* 15, 47. <https://doi.org/10.1186/s13024-020-00396-2>.
38. Di Virgilio, F., Dal Ben, D., Sarti, A.C., Giuliani, A.L., and Falzoni, S. (2017). The P2X7 Receptor in Infection and Inflammation. *Immunity* 47, 15–31. <https://doi.org/10.1016/j.immuni.2017.06.020>.
39. Parvathenani, L.K., Tertyshnikova, S., Greco, C.R., Roberts, S.B., Robertson, B., and Posmantur, R. (2003). P2X7 mediates superoxide production in primary microglia and is up-regulated in a transgenic mouse model of Alzheimer's disease. *J. Biol. Chem.* 278, 13309–13317. <https://doi.org/10.1074/jbc.M209478200>.
40. McLarnon, J.G., Ryu, J.K., Walker, D.G., and Choi, H.B. (2006). Upregulated expression of purinergic P2X(7) receptor in Alzheimer disease and amyloid-beta peptide-treated microglia and in peptide-injected rat hippocampus. *J. Neuropathol. Exp. Neurol.* 65, 1090–1097. <https://doi.org/10.1097/01.jnen.0000240470.97295.d3>.
41. Kowal, J., Arras, G., Colombo, M., Jouve, M., Morath, J.P., Primdal-Bengtson, B., Dingli, F., Loew, D., Tkach, M., and Théry, C. (2016). Proteomic comparison defines novel markers to characterize heterogeneous populations of extracellular vesicle subtypes. *Proc. Natl. Acad. Sci. USA* 113, E968–E977. <https://doi.org/10.1073/pnas.1521230113>.
42. Mathieu, M., Martin-Jaulat, L., Lavieu, G., and Théry, C. (2019). Specificities of secretion and uptake of exosomes and other extracellular vesicles for cell-to-cell communication. *Nat. Cell Biol.* 21, 9–17. <https://doi.org/10.1038/s41556-018-0250-9>.
43. Ai, Y., Guo, C., Garcia-Contreras, M., Sánchez B, L.S., Saftics, A., Shodubi, O., Raghunandan, S., Xu, J., Tsai, S.J., Dong, Y., et al. (2024). Endocytosis blocks the vesicular secretion of exosome marker proteins. *Sci. Adv.* 10, eadi9156. <https://doi.org/10.1126/sciadv.adi9156>.
44. Burk, R.F., and Hill, K.E. (2005). Selenoprotein P: an extracellular protein with unique physical characteristics and a role in selenium homeostasis. *Annu. Rev. Nutr.* 25, 215–235. <https://doi.org/10.1146/annurev.nutr.24.012003.132120>.
45. Hondal, R.J., Ma, S., Caprioli, R.M., Hill, K.E., and Burk, R.F. (2001). Heparin-binding histidine and lysine residues of rat selenoprotein P. *J. Biol. Chem.* 276, 15823–15831. <https://doi.org/10.1074/jbc.M010405200>.
46. Kurokawa, S., Hill, K.E., McDonald, W.H., and Burk, R.F. (2012). Long isoform mouse selenoprotein P (Sepp1) supplies rat myoblast L8 cells with selenium via endocytosis mediated by heparin binding properties and apolipoprotein E receptor-2 (ApoER2). *J. Biol. Chem.* 287, 28717–28726. <https://doi.org/10.1074/jbc.M112.383521>.
47. Baietti, M.F., Zhang, Z., Mortier, E., Melchior, A., Degeest, G., Geeraerts, A., Ivarsson, Y., Depoortere, F., Coomans, C., Vermeiren, E., et al. (2012). Syndecan-syntenin-ALIX regulates the biogenesis of exosomes. *Nat. Cell Biol.* 14, 677–685. <https://doi.org/10.1038/ncb2502>.
48. Joshi, B.S., and Zuhorn, I.S. (2021). Heparan sulfate proteoglycan-mediated dynamin-dependent transport of neural stem cell exosomes in an in vitro blood-brain barrier model. *Eur. J. Neurosci.* 53, 706–719. <https://doi.org/10.1111/ejn.14974>.
49. Christianson, H.C., Svensson, K.J., van Kuppevelt, T.H., Li, J.P., and Belting, M. (2013). Cancer cell exosomes depend on cell-surface heparan sulfate proteoglycans for their internalization and functional activity. *Proc. Natl. Acad. Sci. USA* 110, 17380–17385. <https://doi.org/10.1073/pnas.1304266110>.
50. Baixaui, F., López-Otín, C., and Mittelbrunn, M. (2014). Exosomes and autophagy: coordinated mechanisms for the maintenance of cellular fitness. *Front. Immunol.* 5, 403. <https://doi.org/10.3389/fimmu.2014.00403>.
51. Eitan, E., Suire, C., Zhang, S., and Mattson, M.P. (2016). Impact of lysosome status on extracellular vesicle content and release. *Ageing Res. Rev.* 32, 65–74. <https://doi.org/10.1016/j.arr.2016.05.001>.
52. Alvarez-Erviti, L., Seow, Y., Schapira, A.H., Gardiner, C., Sargent, I.L., Wood, M.J.A., and Cooper, J.M. (2011). Lysosomal dysfunction increases exosome-mediated alpha-synuclein release and transmission. *Neurobiol. Dis.* 42, 360–367. <https://doi.org/10.1016/j.nbd.2011.01.029>.
53. Kwon, H.S., and Koh, S.H. (2020). Neuroinflammation in neurodegenerative disorders: the roles of microglia and astrocytes. *Transl. Neurodegener.* 9, 42. <https://doi.org/10.1186/s40035-020-00221-2>.
54. You, Y., Borgmann, K., Edara, V.V., Stacy, S., Ghorpade, A., and Ikezu, T. (2020). Activated human astrocyte-derived extracellular vesicles modulate neuronal uptake, differentiation and firing. *J. Extracell. Vesicles* 9, 1706801. <https://doi.org/10.1080/20013078.2019.1706801>.
55. You, Y., Muraoka, S., Jedrychowski, M.P., Hu, J., McQuade, A.K., Young-Pearse, T., Aslebagh, R., Shaffer, S.A., Gygi, S.P., Blurton-Jones, M., et al. (2022). Human neural cell type-specific extracellular vesicle proteome defines disease-related molecules associated with activated astrocytes in Alzheimer's disease brain. *J. Extracell. Vesicles* 11, e12183. <https://doi.org/10.1002/jev2.12183>.
56. Saito, T., Matsuba, Y., Mihira, N., Takano, J., Nilsson, P., Itohara, S., Iwata, N., and Saido, T.C. (2014). Single App knock-in mouse models of Alzheimer's disease. *Nat. Neurosci.* 17, 661–663. <https://doi.org/10.1038/nn.3697>.
57. Zhou, Y., Zhou, B., Pache, L., Chang, M., Khodabakhshi, A.H., Tanaseichuk, O., Benner, C., and Chanda, S.K. (2019). Metascape provides a biologist-oriented resource for the analysis of systems-level datasets. *Nat. Commun.* 10, 1523. <https://doi.org/10.1038/s41467-019-09234-6>.

## STAR★METHODS

### KEY RESOURCES TABLE

REAGENT or RESOURCE	SOURCE	IDENTIFIER
<b>Antibodies</b>		
Rat monoclonal anti-Mac-2 (Galectin-3)	Biolegend	Cat#125401; RRID:AB_1134237
Rabbit polyclonal anti-GFP	Novus Biologicals	Cat#NB600-308; RRID:AB_10003058
Goat polyclonal anti-RFP	Rockland	Cat#200-101-379; RRID:AB_2744552
Rat monoclonal anti-P2ry12	Biolegend	Cat#848002; RRID:AB_2650634
Rabbit polyclonal anti-MAP2	Abcam	Cat#ab32454 RRID:AB_776174
Rabbit polyclonal anti-GFAP	Agilent/Dako	Cat#Z033401-2 RRID:AB_10013382
Rabbit polyclonal anti-Hgs	Thermo Fischer	Cat#PA5-27491 RRID:AB_2544967
Mouse monoclonal anti-Lamp1	Santa Cruz Biotech	Cat#sc-20011 RRID:AB_626853
Donkey anti-Rabbit, Alexa Fluor™ 488	Thermo Fischer	Cat#A-21206; RRID:AB_2535792
Donkey anti-Goat, Alexa Fluor™ 594	Thermo Fischer	Cat#A-11058; RRID:AB_2534105
Donkey anti-Rat, DyLight™ 650	Thermo Fischer	Cat#SA5-10029; RRID:AB_2556609
Goat anti-Mouse, Alex Fluor™ 647	Thermo Fischer	Cat#A-21235; RRID:AB_2535804
Goat anti-Mouse, Alex Fluor™ 350	Thermo Fischer	Cat#A-11045 RRID:AB_142754
<b>Bacterial and virus strains</b>		
pLV-EF1 $\alpha$ -mEmerald-CD9-miR9T	Tsuneya Ikezu (Clayton et al., 2021)	Addgene: Cat#170452
LV-CMV-CD63-tdTomato-puro	Ruan et al. 2022	
pLKO.1-puro-CMV-tGFP-scrabble shRNA	Sigma-Aldrich	Non-Target shRNA Control
pLKO.1-puro-CMV-tGFP-Sepp1 shRNA-Clo.1	Sigma-Aldrich	Cat#TRCN0000120685
pLKO.1-puro-CMV-tGFP-Sepp1 shRNA-Clo.2	Sigma-Aldrich	Cat#TRCN0000352521
pLKO.1-puro-CMV-tGFP-Sepp1 shRNA -Clo.3	Sigma-Aldrich	Cat#TRCN0000340550
Lentifect lentiviral particles - EF1 $\alpha$ -puro-mCherry-Sepp1 shRNA	GeneCopoeia	Cat#LPP-MSE094928-LVE004-a-050
Lentifect lentiviral particles - EF1 $\alpha$ -puro-mCherry-scrabble shRNA	GeneCopoeia	Cat#LPP-MSE094928-LVE004-a-050
<b>Chemicals, peptides, and recombinant proteins</b>		
FSB staining solution	Sigma-Aldrich	Cat#07602
Adenosine 5'-triphosphate disodium salt hydrate (ATP)	Sigma-Aldrich	Cat#A6419
Paraformaldehyde	Sigma-Aldrich	Cat#441244
<b>Critical commercial assays</b>		
Lipi-Deep Red	Dojindo	Cat#LD04-10
Lysotracker Deep Red	Thermo Fischer	Cat#L12492
pHrodo™ Deep Red E. coli BioParticles™ Conjugate for Phagocytosis	Thermo Fischer	Cat#P35360
<b>Deposited Data</b>		
Bulk RNA sequencing	SRA/BioProject; <a href="https://www.ncbi.nlm.nih.gov/bioproject/?term=PRJNA1179490">https://www.ncbi.nlm.nih.gov/bioproject/?term=PRJNA1179490</a>	PRJNA1179490

(Continued on next page)

**Continued**

REAGENT or RESOURCE	SOURCE	IDENTIFIER
<b>Experimental models: Cell lines</b>		
BV2 cell line	CABRI	Cat#ICLC ATL03001; RRID:CVCL_0182
<b>Experimental models: Organisms/strains</b>		
Mouse: App <sup>N-L-GF</sup> Apptm3.1Tcs/Apptm3.1Tcs	Takaomi Saido (Saito et al. 2014) <sup>56</sup>	
Mouse: CD-1® IGS Mouse	Charles River Laboratories	strain code 022
<b>Oligonucleotides</b>		
E16WT: 5' -ATCTCGGAAGTGAAGATG-3'	Saito et al. 2014 <sup>56</sup>	
E16MT: 5' -ATCTCGGAAGTGAATCTA-3'	Saito et al. 2014 <sup>56</sup>	
WT: 5' -TGTAGATGAGAACTTAAC-3'	Saito et al. 2014 <sup>56</sup>	
LoxP: 5' -CGTATAATGTATGCTATACGAAG-3'	Saito et al. 2014 <sup>56</sup>	
Sepp1 TaqMan probes	Thermo Fischer	Mm00486048_m1
Gapdh TaqMan probes	Thermo Fischer	Mm99999915_g1
Hgs TaqMan probes	Thermo Fischer	Mm00468635_m1
Vps37b TaqMan probes	Thermo Fischer	Mm01196801_m1
Lamp1 TaqMan probes	Thermo Fischer	Mm01217070_m1
Apoe TaqMan probes	Thermo Fischer	Mm01307193_g1
Selenoprotein P siRNA (m)	Santa Cruz Biotech	Cat#sc-40931
Control siRNA (FITC Conjugate)-A	Santa Cruz Biotech	Cat#sc-36869
<b>Software and algorithms</b>		
GraphPad Prism 9	GraphPad Software Inc.	
BioRender	Biorender	<a href="https://www.BioRender.com">https://www.BioRender.com</a>
Imaris analysis software 9.	Oxford instruments	
CODI	ONI	<a href="https://alto.codi.bio">https://alto.codi.bio</a>
Metascape	Zhou et al. 2019 <sup>57</sup>	<a href="https://metascape.org/">https://metascape.org/</a>
Ingenuity Pathway Analysis	Qiagen	
Incucyte analysis software	Sartorius	
Dr. Tom	BGI	
<b>Other</b>		
DMEM medium	Thermo Fischer	Cat#11965118
Fetal Bovine Serum	Thermo Fischer	Cat#10082147
GlutaMAX™ Supplement	Thermo Fischer	Cat#35050061
Dulbecco's phosphate buffered saline (PBS), no calcium, no magnesium	Thermo Fischer	Cat#14190144
Lipopolysaccharide	Sigma-Aldrich	Cat#L3024
Neural Tissue Dissociation Kit	Milltenyi Biotec	Cat#130-093-231
HBSS, no calcium, no magnesium, no phenol red	Thermo Fischer	Cat#14175095
Neurobasal™ Medium	Thermo Fischer	Cat#21103049
B-27™ Supplement (50X), serum free	Thermo Fischer	Cat# 17504044
Penicillin-Streptomycin (10,000 U/mL)	Thermo Fischer	Cat#15140122
Trypsin-EDTA (0.25%), phenol red	Thermo Fischer	Cat#25200072
siRNA Reagent System	Santa Cruz Biotech	Cat#sc-45064
SuperScript™ IV VLO™ Master Mix kit	Thermo Fischer	Cat#11766050
TaqMan™ Fast Advanced Master Mix	Applied Biosystems	Cat#4444557
Millex-GP Syringe Filter Unit, 0.22 mm	Millipore Sigma	Cat#SLGPR33RS
Puromycin	InvivoGen	Cat#ant-pr-1
miRNeasy Micro Kit	Qiagen	Cat#217084
Triton X-100	Sigma-Aldrich	Cat#T9284

(Continued on next page)

**Continued**

REAGENT or RESOURCE	SOURCE	IDENTIFIER
Normal Donkey serum	Sigma-Aldrich	Cat#D9663
Normal Goat serum	Sigma-Aldrich	Cat#G9023
Costar™ 6-well Clear TC-treated Multiple Well Plates	Corning	Cat#3516
Costar™ 24-well Clear TC-treated Multiple Well Plates	Corning	Cat#3524
96-well Clear Flat Bottom TC-treated Microplate	Corning	Cat#3585
Tissue-Plus™ O.C.T. Compound	Fisher scientific	Cat#SGN4585
Bovine Serum Albumin	Sigma-Aldrich	Cat#A7906
Fluoromount-G™ Mounting Medium, with DAPI	Thermo Fischer	Cat#00-4959-52
TetraSpeck™ Microspheres, 0.1 μm, fluorescent blue/green/orange/dark red	Thermo Fischer	Cat#T7279
BCubed Imaging Buffer	ONI	Cat#900-00004
Silica Nanospheres Cocktail #1 (small EVs; 68–155 nm)	NanoFCM	Cat#S16M-Exo
Silica Nanospheres Cocktail #3 (large EVs; 155–850 nm)	NanoFCM	Cat#S17M-MV
Quality Control Nanospheres	NanoFCM	Cat#QS2503
96-well coverglass bottom plates	Thermo Fischer	Cat#265301
Bulk RNA sequencing	BGI	

## EXPERIMENTAL MODEL AND STUDY PARTICIPANT DETAILS

### Ethical approval and consent to participate

Animals and experimental procedures were approved by the IACUC of Mayo Clinic Florida.

### Animals and genotyping

All mouse care and experimental procedures were approved by Institutional Animal Care and Use Committee of the Mayo Clinic Florida. Pregnant female mice (CD-1) were directly purchased from Charles River Laboratories (strain code 022) for E18 and P1 pups primary culture preparations. *APP<sup>NL-G-F</sup>* mice were bred and genotyped in-house. Mice were caged in accordance with their own sex and housed in a barrier facility with 12 h light and 12 h dark cycles. Food and water were provided *ad libitum*. Throughout the life of all mice, veterinary staff closely monitored animals for complications. Genotyping for animals was conducted in house via PCR using the following primers<sup>9,56</sup>: E16WT: 5′ – ATCTCGGAAGTGAAGATG – 3′ E16MT: ATCTCGGAAGTGAATCTA WT: 5′ – TG TAGATGAGAACTTAAC – 3′ *loxP*: 5′ – CGTATAATGTATGCTATACGAAG – 3′.

### Cell lines

Murine microglia BV-2 cell lines (cat. no. ICLC ATL03001, CABRI) were grown at 37°C in Dulbecco's modified essential medium (DMEM) (Thermo Fisher Scientific, #11965118) supplemented with 10% Fetal Bovine Serum (FBS, Invitrogen, #10082147), 2 mM GlutaMAX Supplement (Thermo Fisher Scientific, #35050061).

## METHOD DETAILS

### Lentiviral vector construction

Both tdTomato and mEmerald DNA sequence, fused to the human CD63 and CD9 genes, respectively, were synthesized and packaged as previously described.<sup>9,22</sup> Briefly, for plasmid construction tdTomato-CD63 sequence was cloned into the pLenti-puro vector (Addgene, #39481) to create the pLenti-tdTomato-CD63 vector, while pLV-EF1α-mEmerald-CD9-miR9T lentivirus was generated by modifying commercially available pLV-PGK-GFP-miR9T vector<sup>36</sup> to contain the murine EF1α promoter and express mEmerald conjugated to CD9 followed by miR9T in the 3′UTR.

### Establishment of EV reporter BV-2 cell lines

BV-2 cells were plated at 50,000 cells/well in 24-well tissue culture plates and allowed to sit down overnight. In the following day, cells were washed twice with PBS and the medium was replaced with fresh media without FBS containing 1 μL of lentiviral particles (pLenti-tdTomato-CD63 or pLV-EF1α-mEmerald-CD9-miR9T) and incubated at 37°C overnight; medium was replaced following incubation. After 48 h post-infection, puromycin (Invivogen, 2 μg/mL) was added to the medium for cell selection of tdTomato-CD63<sup>+</sup> cells. Following lentiviral transduction, cells successfully carrying the tdTomato or mEmerald fluorescent protein were purified using fluorescence-activated cell sorting (FACS) and maintained in regular media.



### Lentivirus transduction of shRNA

All scramble or *Sepp1*-shRNA lentivirus particles ( $10^6$  TU/mL) constructed into the pLenti-puro-CMV-TurboGFP vector were purchased from Sigma-Aldrich. Scramble or *Sepp1*-shRNA lentivirus particles ( $>10^8$  TU/ml) constructed into EF1a-puro-mCherry vector were purchased from GeneCopoeia. TdTomato-CD63<sup>+</sup> and mEmerald-CD9<sup>+</sup> BV-2 cells were transduced with lentivirus particles, as previously mentioned. Following lentiviral transduction, cells successfully expressing the fluorescent TurboGFP were purified using FACS. Cells expressing mCherry were selected using puromycin. Stable double fluorescent cells were then expanded in complete culture medium and stored for further experiments.

### Isolation of the EV-enriched fraction

BV-2 cells were plated at 500,000 cells/well in 6-well tissue culture plates and allowed to sit down overnight. Cells were washed twice with double-filtered PBS (MF-Millipore Membrane Filter, 0.22  $\mu$ m) to remove serum factors, and the medium was replaced with fresh conditioned medium containing double-filtered DMEM (MF-Millipore Membrane Filter, 0.22  $\mu$ m) without FBS. Cells were exposed to 1 mg/mL LPS (Sigma-Aldrich, Cat. L3024) for 3 h followed by 5 mM ATP stimulation for 15 min. Conditioned medium (CM) was collected and enriched for EVs by sequential centrifugation, as previously described.<sup>21</sup> Briefly, the CM was centrifuged at 300 g for 10 min, 2,000 g for 10 min and 10,000 g for 30 min at 4°C. The resulting supernatant was kept as EV enriched CM fraction for nano-flow cytometry or further processed for EVs isolation by ultracentrifugation at 100,000 g for 70 min at 4°C. EV pellet was resuspended in PBS and stored at  $-80^{\circ}\text{C}$  until further use for dSTORM analysis. This method was previously described by our group to generate an enriched EV population under ATP stimulation without any presence of intracellular organelles contaminants.<sup>22</sup>

### Nano-flow cytometry (NanoFCM)

Size and concentration of EVs in BV-2 microglia CM were analyzed using nano-flow cytometry (Flow NanoAnalyzer, NanoFCM). Three mL of EV enriched CM from BV-2 cells treated for 3 h with LPS followed by 15 min ATP were collected and processed as aforementioned for EV isolation and stored overnight at 4°C. After calibration using concentration and small size beads of Flow NanoAnalyzer, 20  $\mu$ L of CM were initially loaded and boosted for 45 s at 1 kPa pressure, followed by 1 min of data acquisition.

### Single molecule super-resolution microscopy

For single molecule imaging of TdTomato-CD63<sup>+</sup> or mEm-CD9<sup>+</sup> tetraspanins on EVs we applied direct stochastic optical reconstruction microscopy (dSTORM) using the super-resolution microscope ONI (Nanoimager S, Oxford Nanoimaging, UK) equipped with a 100X oil-objective (1.4 numerical aperture). The Nanoimager was calibrated before each imaging session using 100 nm fluorescent microspheres (TetraSpeck, Cat. T7284, Invitrogen) to align 405/473/561/640 nm fluorescent channels. For imaging, EVs were diluted at 1:1 ratio using BCubed Imaging Buffer (ONI, Cat. 900-00004) to a final concentration of  $2.5 \times 10^8$  particles in 5  $\mu$ L. The samples were applied to glass slides, mounted with coverslips, and incubated at RT for 5 min in the dark before imaging. TdTomato fluorescence imaging was acquired under 20% power on 561 laser channel and a total of 2000 frames were captured using a 30° total internal reflection fluorescence (TIRF) illumination angle to obtain optimal signal/noise ratio. Images were processed and analyzed using CODI online platform from ONI (<https://alto.codi.bio/>) including filtering and drift correction. TdTomato<sup>+</sup> molecules were clustered using automated BD Scan function and clusters with at least 5 individual molecules were used for analysis.

### Confocal live imaging

BV-2 microglia expressing mEm-CD9 were plated at 10,000 cells per well in 96 wells cover glass bottom plates and incubated overnight in DMEM supplemented media. Media containing 5 mM ATP was added immediately before imaging. Confocal images were taken using SP8 laser confocal microscope (Leica). Videos were acquired by serial imaging for 5 min using 40 $\times$  oil immersion/1.3 NA objective at a pinhole of 1.0 airy and a system-optimized z stack interval of 0.25  $\mu$ m.

### Stereotaxic surgery

*APP<sup>NL-G-F</sup>* mice at 6 months old were deeply anesthetized with isoflurane and immobilized in a mouse stereotaxic frame (David Kopf Instruments) installed with robotic stereotaxic injection system (Drill and Injection Robot, Neurostar). Animals were bilaterally injected with 1  $\mu$ L of pLV-EF1 $\alpha$ -mEmerald-CD9-miR9T lentiviral particles (Viral titer:  $>10^9$  TU/ml) into the hippocampus (AP:  $-2.18$  mm; ML: 1.9 mm; DV:  $-1.3$  mm from the skull). After two weeks, the animals were injected into the same hippocampal coordinate with 1  $\mu$ L lentivirus particles (Viral titer:  $>10^8$  TU/ml) for expression of mCherry-Scramble-shRNA or *Sepp1*-shRNA (GeneCopoeia). Mice were euthanized at two weeks post-injection for immunohistochemical analyses.

### Histological processing and immunofluorescence staining

Brains were harvested after transcardial perfusion with ice-cold PBS followed by post-fixation in 4% PFA overnight at 4°C. The following day, brains were transferred to cryoprotection solution containing 30% sucrose in PBS and incubated for two days at 4°C, and then embedded in O.C.T. compound (Fisher Scientific, 23-730-571) for coronal cryosectioning at 30- $\mu$ m thickness using a cryostat. The following antibodies and reagents were used for immunofluorescence staining: GFP 1:500 (Novus Biologicals, #NB600-308), Mac-2 1:300 (Galectin-3, Biolegend, #125401), RFP 1:500 (Rockland, #200-101-379), P2ry12 (Biolegend, #848002) and Alexa Fluor secondary antibodies 1:1000 (Thermo Fischer Scientific). Sections were washed with PBS for 10 min prior to be

incubated with blocking solution (5% normal donkey serum, 5% bovine serum albumin (BSA), and 1% Triton X-100) for 1 h at RT. Antibody staining buffer consisted of 5% BSA, 1% Triton X-100 in PBS. Primary and secondary antibody staining were performed overnight at 4°C and for 1 h at RT, respectively. Following staining, sections were washed with PBS and then mounted using Fluoromount-G with DAPI (Invitrogen, # 00-4959-52). Confocal images were taken using SP8 laser confocal microscope with Lightning (Leica). Images from mEm-CD9<sup>+</sup> particles were taken using 63× oil immersion/1.4 NA objective, and 3.69 optical zoom (size is around 50-μm by 50-μm) at a pinhole of 1.0 airy unit. Confocal microscopic imaging stacks of images with 1024 × 1024-pixel resolution were collected while using a system-optimized z stack interval of 0.25 μm. Processing of z stack images and quantification of mEm-CD9<sup>+</sup> particles was accomplished using IMARIS rendering software (Oxford Instruments).

### RNA isolation and bulk RNA sequencing

Total RNA from BV-2 microglia was extracted using miRNeasy Plus Micro Kit (Qiagen, 217084) according to the manufacturer's protocol for purification of total RNA containing small RNAs from cells. Equal 200 ng of RNA for each sample were used for cDNA library construction and sequencing performed by BGI using the DNBSEQ platform with a sequencing depth of 40 million reads per sample. The sequencing data were filtered using SOAPnuke 1.5.2 software, and the clean reads were mapped to a reference genome using HISAT2 2.0.4 software. After alignment using Bowtie2 2.4.4 software, the expression level of each gene was calculated by RSEM 1.2.28 software. Samples had >44.8 million mapped reads with an average of 93.68% (93–94.9% range) of reads mapped to the mouse genome. The average alignment of the gene set was 79.05% (77–81% range) and a total of 16021 genes were detected. Differential expression analysis was performed using DESeq2 package with *q*-value ≤ 0.05.

### Bioinformatic and pathway analysis

The sequencing data was analyzed using Dr. Tom software from BGI. Common DEGs which were found to be regulated by at least two *Sepp1*-ShRNA clones were applied for pathway analysis. Gene annotation was performed based on gene ontology (<http://www.geneontology.org/>) and KEGG pathway (<https://www.kegg.jp/>) analysis of DEGs with *q*-value ≤ 0.05. Top ranked DEGs were applied to Metascape (<http://www.metascape.org>)<sup>57</sup> software for pathway enrichment analysis. Common regulated *Sepp1*-DEGs along with their corresponding fold changes and *Q*-values were analyzed using the ingenuity pathway analysis (IPA) software. Canonical pathways and biological functions were tested for prediction of molecular networks.

### Live imaging of cell phagocytosis, lipid accumulation and lysosome monitoring

BV-2 microglia cells were plated at 10,000 cells per well in 96 wells plates and incubated overnight in DMEM supplemented media. Cells were washed twice with PBS and new supplemented media containing 200 nM LysoTracker Deep Red (Thermo Fischer Scientific, #L12492), 0.5 μM Lipi-Deep Red (Dojindo, #LD04-10) or 1 μg/mL pHrodoDeep Red E. coli BioParticles (Thermo Fischer Scientific, #P35360) were added. Bright field and fluorescence images were acquired using Incucyte S3 Zoom HD/2CLR time-lapse microscopy system (Sartorius) set up in a humidity chamber at 37°C and 5% CO<sub>2</sub>. Each well was divided into 9 imaging fields and images were acquired every 1 h for 6 h using a 20× objective. Images were processed using the basic analysis function on Incucyte analysis software and total integrated intensity within cells were calculated and normalized by confluence for each time point.

### Primary cell culture

Primary cortical cultures of neurons and astrocytes were prepared from CD-1 mouse brains at E16 or P1 pups, respectively. Briefly, brain tissue was isolated and transferred to iced-cold HBSS (Gibco, #14175095). Cortices were dissected for meninges removal, minced and dissociated by enzymatic digestion using a Neural Tissue Dissociation Kit (Miltenyi Biotec, #130-093-231). Cortical neurons were plated on poly-D-lysine (Sigma-Aldrich, #A-003-M) pre-coated 24 well dishes at a density of 200,000 cells in Neurobasal medium (Gibco, #21103049) containing 2% B27 (Gibco, #17504044), 2 mM Glutamax (Gibco Invitrogen, #35050061) and 1% penicillin/streptomycin (P/S, Gibco, #15140122) with half medium replacement every 3 days. For astrocytes cultures, cells were plated on poly-D-lysine pre-coated 75-cm<sup>2</sup> flasks at a density of 1 × 10<sup>7</sup> cells in DMEM containing 10% FBS and 1% P/S with medium replacement every other day. After 10 days, non-astrocytic cells were removed by shaking at 250 rpm for 1 h and washed twice with PBS. Astrocytic cells in the monolayer were detached using trypsin-EDTA 0.25% (Gibco, 25200072) and replated on 24 well dishes at a density of 150,000 cells. Primary neurons (DIV10) and astrocytes (DIV11) cultures were gently washed and transduced with siRNA pools targeting *Sepp1* (Santa Cruz Biotech., #sc-40931) or scrambled sequence (Santa Cruz Biotech., #sc-36869) using the siRNA Reagent System from Santa Cruz Biotech (#sc-45064). After 5 h incubation, cells were washed and incubated for 48 h in regular basal medium until stimulation with LPS and ATP as described for isolation of EV-enriched CM fraction. The cell pellet was collected for RNA isolation.

### qRT-PCR analysis

Total RNA from cells was reverse transcribed using SuperScript IV VILO Master Mix kit (Thermo Fisher Scientific, #11766050). Quantitative PCR was performed using Taqman probes with TaqMan Fast Advanced Master Mix (Applied Biosystems, #4444557). Relative amounts of mRNA were calculated after normalization of target genes Ct values to housekeeping gene (Gapdh) Ct value.

### Immunocytochemistry (ICC)

Cells were washed PBS and fixed in 4% PFA for 15 min at RT. Cells were permeabilized and blocked in a blocking solution (5% normal goat serum, 5% bovine serum albumin (BSA), and 1% Triton X-100) for 1 h at RT. Primary and secondary antibody staining were performed overnight at 4°C and for 1 h at RT, respectively. The following antibodies and reagents were used for immunofluorescence staining: MAP2 1:250 (Abcam, #ab32454), GFAP 1:250 (Agilent, Z033401-2), Hgs 1:250 (Thermo Fisher, #PA5-27491), Lamp1 1:250 (Santa Cruz Biotech, #sc-20011) and Alexa Fluor secondary antibodies 1:1000 (Thermo Fischer Scientific). Following staining, cells were washed with PBS and then mounted using Fluoromount-G (Invitrogen, # 00-4958-02). Confocal images were taken using SP8 laser confocal microscope with Lightning (Leica).

### QUANTIFICATION AND STATISTICAL ANALYSIS

All data are presented as the mean  $\pm$  standard error of the mean (SEM). Two-tailed unpaired Student's *t*-tests were used for comparisons between the two groups. Multiple comparisons were performed using either one-way ANOVA, followed by Holm-Šidák post hoc tests. Statistical analyses were performed using Prism 9.3.1 (GraphPad Software). Statistical significance was set as  $p < 0.05$  or as stated at figure legends. For transcriptomics analysis significance was eventually set as FDR corrected *p*-value (*q*-value).